ANNUAL REVIEWS

Annual Review of Fluid Mechanics

Moisture in Textiles

C. Duprat

Hydrodynamics Laboratory, Department of Mechanics, Ecole Polytechnique, Institut Polytechnique de Paris, Palaiseau, France; email: camille.duprat@polytechnique.edu

Annu. Rev. Fluid Mech. 2022. 54:443–67

First published as a Review in Advance on November 8, 2021

The *Annual Review of Fluid Mechanics* is online at fluid.annualreviews.org

https://doi.org/10.1146/annurev-fluid-030121-034728

Keywords

textile, paper, fiber, capillarity, elastocapillarity, wetting, wicking, imbibition

Abstract

The interactions of textiles with moisture have been thoroughly studied in textile research, while fluid mechanists and soft matter physicists have partially investigated the underlying physics phenomena. A description of liquid morphologies in fibrous assemblies allows one to characterize the associated capillary forces and their impact on textiles, and to organize their complex moisture transport dynamics. This review gathers some of the common features and fundamental mechanisms at play in textile–liquid interactions, with selected examples ranging from knitted fabrics to nonwoven paper sheets, associated with experiments on model systems.

1. INTRODUCTION

Yarn: short (staple) or continuous (multifilament) fibers, mostly parallel, held together by friction by introducing twist; increasing twist or applying tension produces lateral compression, aligning and holding fibers and making the yarn more compact

Textiles, or more generally thin fibrous media, are ubiquitous in natural and engineered systems, and research on textiles has been driven by a large variety of applications. Textile fibers are often hygroscopic, i.e., can absorb water from the moist atmosphere, and, in many situations, may also interact with liquids, which is the situation we examine in this review. The presence of liquid and, in particular, of liquid–air interfaces may provide strong interfiber forces. A simple illustration of these forces consists of moistening the end of a thread before threading a needle: Capillarity provides sufficient interfiber forces to stick the strands of the thread together, thus increasing its stiffness (Skelton 1975, Py et al. 2007). The development of such large forces is particularly relevant in paper making, where cellulose fibers are put into close molecular contact upon dewatering of the initial pulp suspension (**Figure 1*a***). When a piece of paper is rewetted, the imbibition front is not sharp (**Figure 1*b***); water can further penetrate and swell the fibers themselves, leading to large-scale deformations upon wetting and drying, such as out-of-plane wrinkles, crinkles, and irreversible shrinkage (Balankin et al. 2006, Bosco et al. 2018, Ostlund 2018). The spreading of drops of dye or stains on fabrics exhibits intricate patterns (**Figure 1*c–e***), and washing/drying cycles may affect the overall size and structure of a garment. Modeling the mechanical properties of fibrous materials is a rich multiscale and multiphysics problem (Durville et al. 2018). In particular, the presence of liquid can drastically affect these mechanical properties at all scales; for example, it can increase the strength of wetted yarn (Das et al. 2009) or modify the mechanical response of paper or biocomposite nonwoven materials (Alava & Niskanen 2006, Gager et al. 2019). The sometimes dramatic effect of water on textiles involves an interplay of various physical mechanisms, including elasticity, capillarity, and geometry/topology, at different length scales and timescales. In this review, we highlight some of the common features of textile–liquid interactions, with selected examples ranging from knitted fabrics to nonwoven paper sheets, juxtaposed with simple experiments on model systems.

2. A MULTISCALE PROBLEM

Whether they are woven, knitted, or nonwoven, textiles come in a variety of shapes and have a variety of uses. They are composed of single filaments or yarns made of fibers of different lengths.

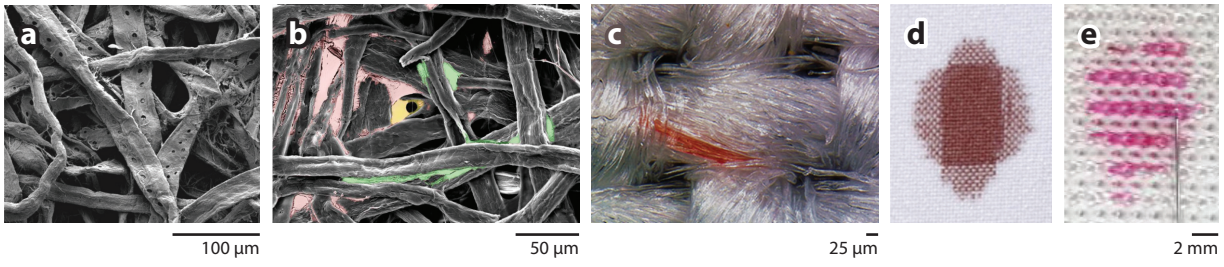

Figure 1

(*a*) SEM (scanning electron microscope) image of a sheet of paper during formation, where cellulose fiber–fiber contacts and fine mattings have been initiated by capillary forces. Panel *a* adapted from Belle & Odermatt (2016) (CC-BY 4.0). (*b*) Cryo-SEM image of a rewetted sheet of paper, with liquid distributed in fully (*red*) or partially (*yellow*) filled pores, as well as in films along fibers (*green*). Panel *b* adapted with permission from Roberts et al. (2003). (*c*) A drop of ink spreading between the filaments of a yarn in a woven textile. Panel *c* adapted with permission from Zhang et al. (2020). (*d*) A drop of blood imbibing in a fabric exhibits a nonuniform spreading pattern with a diffuse front where the liquid mostly invades the warp yarns. Panel *d* adapted with permission from de Castro et al. (2016). (*e*) The spreading of dyed water injected (with a needle) in one yarn of a polyester-polyethylene-blended interlock-knitted fabric as it wicks in the wale and course directions. Panel *e* adapted with permission from Kim et al. (2020).

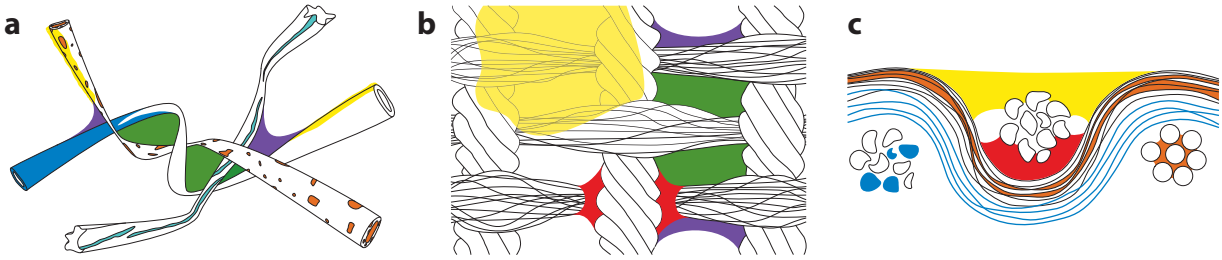

Figure 2

Liquid morphologies of textiles. (*a*) A nonwoven textile, showing various fibers and their cross sections, which are sometimes hollow. (*b*) The top view and (*c*) a cross section of a woven textile. Liquid may be present between fibers or yarns, fully filling (*green*) or partially filling (*purple*) the pores; as films along fibers or on top of the structure (*yellow*); in crevices or crenelations of irregular fibers (*light blue*); between filaments of a yarn, in intrafiber pores, or in the fiber lumen (*orange*); in the contact area between weft and warp yarns (*red*); and within fibers (*blue*).

The fibers themselves may exhibit various cross sections and come from many natural or synthetic materials, including cotton, viscose, nylon, cellulose, glass, and polyester (PET). Nonwoven textiles consist of entangled fibers that are bonded through entanglements and friction, thermal treatment, or a bonding agent (**Figures 1*a*,*b*** and **2*a***). Woven fabrics are made of yarns interlaced in a weave pattern with warp and weft directions (**Figures 1*c*,*d*** and **2*b*,*c***). Knitted fabrics are made from interlocked loops of one or more yarns with wale and course directions (**Figure 1*e***). Different areas of various length scales may be wetted when textiles are exposed to liquids, or when a wet textile is dried (**Figure 2**): Liquid may be found between fibers, either between filaments in a yarn or between yarns; in films and crevices along the fiber; or inside the fibers, either in intrafiber pores, in the lumen of hollow fibers (e.g., cellulose or cotton), or within the material (e.g., the swelling of cellulose with water). The liquid may also spread on the surface of the textile: The weave or knit pattern, the fiber geometry, and the presence of fine hairiness lead to a multiscale surface roughness that impacts the apparent contact angle θ_{app} (Melki et al. 2019). These phenomena (imbibition between fibers, diffusion in the fibers, wicking in crevices on the fibers' surfaces, evaporation from the fibers' surfaces, drainage from the interyarn pores, etc.) are associated with different timescales. The next section describes the amount and morphology of liquid present between fibers and yarns, and highlights the capillary forces generated by the associated interfaces. Section 4 presents the impact of these forces on textiles. Finally, we characterize the imbibition dynamics and, in particular, the consequences of the multiple length scales and timescales presented here.

Warp: lengthwise yarns in a woven textile

Weft: crosswise yarns in a woven textile

Wale: loops running lengthwise in a knitted fabric

Course: loops running crosswise in a knitted fabric

Apparent contact angle θ_{app}: global contact angle of the liquid on the textile, which depends on the underlying geometry and roughness

Wicking: the spontaneous imbibition of liquid within the textile due to capillary forces only

Moisture content ϕ (%): ratio of the mass of liquid m_w within a textile of mass m_t, $\phi = \frac{m_w}{m_t} \times 100$; conversely, we may define the solids content as $\phi_s = 100 - \phi$

3. CAPILLARITY IN FIBROUS ASSEMBLIES

Let us consider a fully wetted fibrous assembly (i.e., a wetted textile or a pulp suspension in the early stages of papermaking), from which liquid is progressively removed (through drainage or drying). For solid contents below 10–15% (i.e., moisture content $\phi > 85\%$), fibers are surrounded by liquid; surface tension forces only operate on the outer surface and the fibrous assembly becomes more compact. Upon further dewatering ($85\% > \phi > 50\%$), air starts penetrating the assembly, fills the larger pores, and liquid–air interfaces appear. At this stage, fibers are connected by capillary bridges, first spanning several fibers, then confined to isolated bridges between fibers and at fiber intersections. Interfiber capillary forces then play an important role, as evidenced by force measurements at the scale of a single fiber in an assembly (Skelton 1975) and between two wet paper sheets [which actually present a maximum force around $\phi = 60\%$, as discussed by van de Ven (2008)], and by the initial wet web strength of paper (Belle & Odermatt 2016). These forces

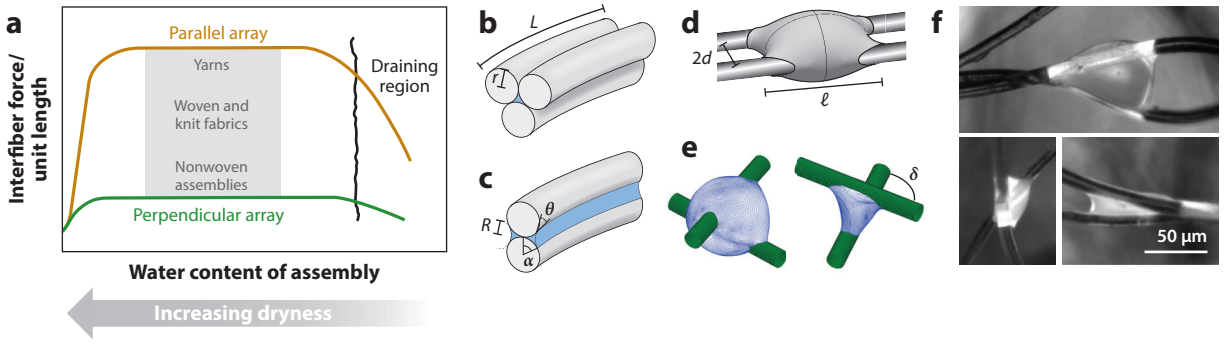

Figure 3

(*a*) The development and magnitude of interfiber capillary forces as a function of moisture content. Panel *a* adapted with permission from Skelton (1975). (*b–d*) Parallel fibers: (*b*) a triangular close packing of cylindrical fibers between which liquid is present (*blue*); (*c*) a cusp-shaped liquid film between two cylindrical fibers; and (*d*) a drop bridging two parallel fibers, obtained numerically with Surface Evolver by Naima Hammoud, following the method described in Bedarkar et al. (2010). (*e,f*) Perpendicular fibers: (*e*) liquid bridges at the intersection of two fibers, obtained numerically with Surface Evolver, and (*f*) fluorescence images of dyed water droplets on a polyester nonwoven fiber. Panel *e* adapted with permission from Soleimani et al. (2015).

Contact angle θ: local contact angle of the liquid on a single fiber, which depends only on the liquids and the materials involved

Capillaries: narrow channels in which liquid can wick or be trapped by capillary forces, in analogy with small vessels through which blood is transported

Linear density *c*: mass per unit length in grams for 10 km of thread/yarn; $c \sim$1–20 dtex

Fineness: fiber radii $r \sim 10$ µm, often expressed as the linear density c via the relation $c = \rho_f \pi r^2$

Fiber density: $\rho_f \sim$ 1–10 g/cm^3

Fiber length: $L \sim$ 1–10 cm for staple fibers and practically infinite for filaments

can be directly observed as fibers are drawn together upon drying of a waterlogged mass of fibers (Morton & Hearle 2008). At higher drynesses ($50\% > \phi > 30\%$), liquid is mostly present within the fibers (in the lumen and intrafiber pores), where capillary forces also play a role and act to close lumens and pores; for lower moisture contents the fibers themselves start to dry. This process is illustrated in **Figure 3*a***. The interfiber forces strongly depend on the fiber and packing geometry. In particular, fiber–fiber contacts are essentially parallel in yarns, while contacts between yarns in a woven fabric, or between fibers in a nonwoven textile, are mostly perpendicular. For simplicity, and as a first model to characterize liquid morphologies and interfiber forces, we consider cylindrical fibers of radius r, wetted by a liquid of surface tension γ with a contact angle θ (**Figure 3*b–e***). We define the dimensionless interfiber distance $2\tilde{d} = 2d/r$ and the dimensionless wetted length $\tilde{\ell} = \ell/r$, corresponding to a dimensionless cross-sectional area of filled capillaries or liquid films $\tilde{A} = A/r^2$, a dimensionless radius of curvature $\tilde{R} = R/r$, and a dimensionless volume $\tilde{V} = V/r^3$, where every quantity is made dimensionless using the fiber radius r.

3.1. Liquid Retention

At the scale of a textile, a first estimate of the liquid distribution and interfiber forces can be obtained by measuring the global amount of liquid held by capillary forces against external forces such as gravitational drainage, centrifugal forces, or suction pressure. During centrifuging, the amount of liquid retained between fibers m_w is indeed given by a balance between acceleration $m_w G$ and capillary forces $p\gamma\cos\theta$, where p is the perimeter wetted by liquid (Morton & Hearle 2008). A generally accepted minimal model of a yarn (and by extension of many textiles) consists of an array of parallel fibers whose packing forms narrow channels in which liquid can be held by capillary forces, often called capillaries (**Figure 3*b,c***). The wet perimeter of such small spaces between fibers, shown in **Figure 3*b***, can be estimated as $p = 2\pi r = 2\sqrt{\pi c/\rho_f}$ for a close packing, where c is the linear density related to the fineness r and ρ_f is the fiber density, while the total fiber mass is given by $m_f = cL$, where L is the fiber length. The liquid retention may thus be expressed as

$$\frac{m_w}{m_f} \sim \frac{\gamma\cos\theta}{GL\sqrt{c\rho_f}}, \qquad 1.$$

as described by Preston et al. (1951) and Morton & Hearle (2008). The linear dependence on $\gamma \cos\theta / G$ is well documented, as is the decrease of holding capacity with increasing density (Preston et al. 1951, Steiger & Kapur 1972, Salehi Rad et al. 2013). The retention decreases when fibers are randomized (i.e., are less parallel), although this expression is still valid for nonwoven textiles (Salehi Rad et al. 2013). Typically, for a PET fabric ($\rho_f = 1.39$ g/cm^3, $L = 70$ mm) wetted by water ($\gamma = 71$ mN/m, $\theta = 72°$), the liquid retention varies from 60% at $c = 3.3$ decitex (dtex) to 20% at $c = 13.3$ dtex after centrifugation at $G = 233$ cm/s^2 (Salehi Rad et al. 2013). The liquid may be held in cusp-shaped films between adjacent fibers (**Figure 3*c***), and the shape of these films can be estimated by applying a suction pressure to the wet fibrous assembly. Indeed, the resulting dewatering is then resisted by the Laplace pressure, γ / R. Typically, most of the liquid is removed for pressures of 10^5 Pa, corresponding to radii of curvature of $R \sim 0.5$ μm, while 10–50% is retained at 10^4 Pa ($R \sim 5$ μm), and the textile remains full for $P \sim 10^3$ Pa ($R \sim 50$ μm), which is consistent with fiber radii between 7 and 200 μm in typical considered textiles (Preston & Nimkar 1952). The amount of liquid held, i.e., the cross-sectional area of the liquid film A, is related to the fiber radius r, the radius of curvature R, and contact angle θ through geometrical arguments, in particular through the spreading angle α (**Figure 3*c***). The amount of retained liquid thus greatly depends on both γ and θ. For example, the amount of water held by nylon fibers ($\gamma = 72$ mN/m, $\theta = 45°$) does not change when a wetting agent is added; indeed, the agent favors wetting by setting a zero contact angle but also reduces the surface tension ($\gamma = 36$ mN/m, $\theta = 0$) (Preston & Nimkar 1952). For noncylindrical fibers, such as wool or cotton, water may be retained in the crevices of the highly convoluted fibers, increasing the overall water retention (Hsieh et al. 1992). In loose nonwoven textiles, liquid may form large drops at fiber intersections (**Figure 3*e*,*f***), as seen in wax droplets solidified during centrifuging (Hearne & Nossar 1983) or binders polymerized on glass wool (Bintein 2015, Sauret et al. 2015). In these cases, the retained volumes and, thus, the associated capillary forces are still proportional to γ and θ but greatly depend on the complex drop and fiber geometry (Hearne & Nossar 1983, Bedarkar et al. 2010, Soleimani et al. 2015). These shapes and the associated forces are particularly important for textiles used as aerosol filters, as they influence both the liquid capture and drop reentrainment (Mullins et al. 2004, Mead-Hunter et al. 2014). Finally, more liquid can be held by stiff fibers, as stiffness diminishes the tendency of fibers to be drawn together and thus maintains a greater interfiber capillary volume, an effect we describe below (Gottlieb et al. 1958, Steiger & Kapur 1972).

Critical distance d_c: the distance below which liquid can wick between fibers, corresponding to $\alpha = \pi/2$; in total wetting ($\theta = 0$), $d_c/r = \pi/2 - 1 \simeq 0.57$

3.2. Liquid Morphologies

At the fiber scale, the simplest system to consider consists of two parallel fibers separated by a distance $2d$. This two-fiber system only acts as a capillary (i.e., liquid spontaneously wicks in between the fibers) below a critical distance d_c, as shown in **Figure 4*a***(Minor et al. 1959b, Miller et al. 1967). This critical distance is evidenced in the experiment shown in **Figure 4*b***, first proposed by Miller et al. (1967) and Dyba & Miller (1969). Two fibers are mounted under tension to form a V shape and dipped into a liquid bath; by lowering the edge of the V, one can easily vary the interfiber distance b in contact with the liquid bath and monitor the height h_i at which the liquid rises between the fibers above the meniscus that forms around the fibers. The critical value of b for the liquid to start imbibing, b_c, depends linearly on the fiber radius and decreases quickly with increasing contact angle (Minor et al. 1959b). This simple experiment was actually proposed as a way to measure the contact angle of liquid on fibers (Princen 1970b). Placing a drop on two fibers and finely varying the interfiber space reveal a transition that presents a hysteresis (**Figure 4*c***). Starting from a compact semispherical drop, the liquid spreads between the fibers at a critical distance d_{c*} to form a long column that appears to be of uniform cross section. With an

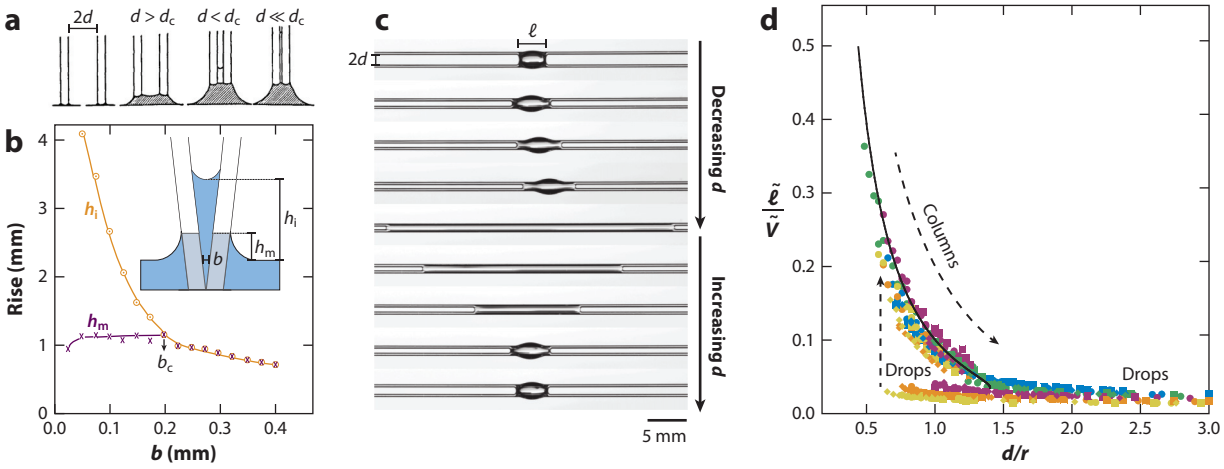

Figure 4

(*a*) Liquid rise between two parallel fibers. The liquid always rises around the fibers as an outside meniscus (*shaded region*) and rises between the fibers (*white region*) only if the interfiber distance is lower than a critical distance d_c. (*b*) Rise of mineral oil between V-shaped nylon fibers ($2r = 0.5$ mm), showing the height of the outside meniscus (h_m) and of the meniscus between the fibers (h_i). The height of the outside meniscus h_m is limited by gravity and saturates at a height of ∼1.2 mm. The liquid rises between the fibers ($h_i > h_m$) for $b < b_c = d_c$ and h_i increases with decreasing interfiber distance b. Panels *a* and *b* adapted with permission from Dyba & Miller (1969). (*c*) Spreading and retraction of a totally wetting drop (silicone oil; contact angle $\theta = 0$) on two horizontal parallel nylon fibers ($2r = 0.4$ mm) as the interfiber distance is varied. (*d*) Evolution of the inverse of the cross-sectional area $\tilde{A}^{-1} = \tilde{\ell}/\tilde{V}$ of a wetting drop between two horizontal parallel fibers for various fiber diameters and drop volumes (Protière et al. 2013). All data for columns collapse onto a single curve—i.e., increasing the volume increases the column length but does not change its cross-sectional shape. These columns exist up to $d_{m^*} \simeq 1.4$. Panel *d* adapted with permission from Protière et al. (2013).

increasing interfiber distance, the liquid remains as a column whose length slowly decreases until reaching another critical distance, d_{m^*}, at which it gathers back as a drop (Protière et al. 2013). By plotting the evolution of the inverse of the liquid cross-sectional area $\tilde{A} = \tilde{V}/\tilde{\ell}$ for different interfiber distances, we can organize the data into two distinct trends (**Figure 4*d***); while drops form a lower scattered branch, liquid columns collapse onto a single curve, indicating that there is a unique column shape of constant cross section $\tilde{A}$ that solely depends on the interfiber distance d/r, which was first described by Princen (1970a).

Neglecting the menisci at the edges of the column, the shape of the column is characterized by the angle α and the radius of curvature R, as shown in **Figure 5*a***. A force balance on a small volume $\mathrm{d}V = A\,\mathrm{d}L$ yields

$$4r\alpha\gamma\cos\theta - 4\gamma R\left(\frac{\pi}{2} - \theta - \alpha\right) - \gamma\frac{A}{R} = 0, \qquad 2.$$

where the terms from left to right correspond, respectively, to the force at the fiber–liquid surface, the force at the free surface, and the force originating from the Laplace pressure γ/R in the column. Combining this force balance equation with geometric arguments allows one to fully describe the shape of the liquid (i.e., α and $\tilde{R}$) as a function of the distance $\tilde{d}$. As $\tilde{d}$ increases, α increases, i.e., the liquid spreads around the fibers, and the section evolves from a convex inward interface with $\alpha < \pi/2$ and $\tilde{R} > 0$ to a concave outward area with $\alpha > \pi/2$ and $\tilde{R} < 0$ (**Figure 5*b***). The existence of these concave columns was confirmed by Princen (1970a), who performed experiments with large fibers immersed in a fluid to prevent any gravitational effects (**Figure 5*c***). These columns may only exist up to a maximum distance d_m, where $\alpha = \pi$ [i.e., the liquid completely surrounds the fibers and the column has a circular cross section, $\tilde{R} = -(2 + \tilde{d})$]. If the distance

Maximum distance d_m: the maximum distance below which columns may be formed, corresponding to $\alpha = \pi$; in total wetting ($\theta = 0$), $d_m/r = \sqrt{2}$

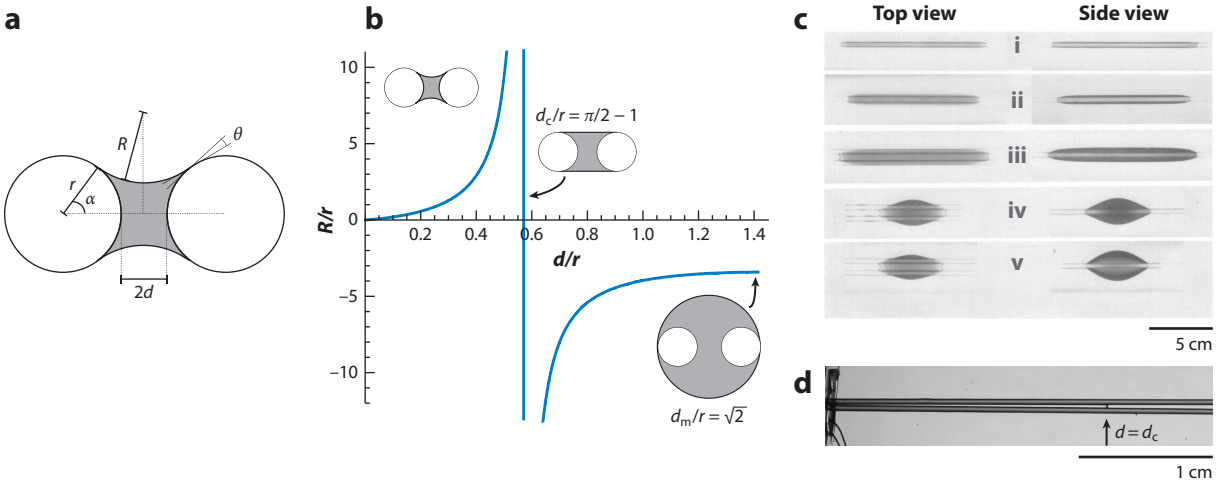

Figure 5

Shapes of liquid columns. (*a*) A cross section of a liquid column between two fibers. (*b*) The evolution of the radius of curvature R/r of a column as the interfiber distance is varied in total wetting ($\theta = 0$). (*c*) Pictures of dyed water columns and drops on glass rods ($2r =$ 4 mm) immersed in butyl benzoate (with drop of dyed water with salt and surfactant to ensure isodensity and $\theta = 0$), at distances (*top to bottom*) $\tilde{d} = d/r = 0.68$ (*i*), 1.025 (*ii*), 1.270 (*iii*), 1.270 (*iv*), and 1.424 (*v*). Panel *c* adapted with permission from Princen (1970a). (*d*) Imbibition between two horizontal fibers, forming an angle whose tip is placed in a bath. The liquid stops at $d = d_c$. Panel *d* adapted with permission from Bintein (2015).

between the fibers is further increased, it is no longer possible to form a column, and only drops may prevail, as seen in **Figure 4*d***. At $d = d_c$, we have $\alpha = \pi/2$ and the interface is flat (i.e., $R \to \infty$). The value d_c thus corresponds to the critical distance below which liquid will spontaneously wick in between the fibers, which can be evidenced further by looking at spontaneous imbibition between two fibers forming an angle (Bintein 2015). In such cases, the liquid will imbibe as long as there is a pressure difference between the bath at atmospheric pressure and the liquid column, i.e., for $R > 0$: The imbibition front thus stops at a length for which $d = d_c$, which has indeed been observed in experiments (**Figure 5*d***). For $d < d_c$, the convex columns are stable and thus prevent the growth of drops; indeed, the Plateau–Rayleigh instability does not appear on adjacent parallel fibers (Wang et al. 2020), and incoming droplets immediately coalesce with liquid columns, creating, for example, efficient superhydrophilic fibers for aerosol collection (Labbé & Duprat 2019). Between d_c and d_m, the column shape is metastable at large volumes (**Figure 6*a***) and drops are favored, as their surface energy is lower than that of a spread column (Protière et al. 2013). The existence regions of drops, concave columns, or convex columns also depend on contact angle (**Figure 6*b***) (Lukáš et al. 2006); in partial wetting, small distances must be reached for wicking to occur between fibers, even for moderate contact angles ($\theta < 45°$).

In textiles, fibers are not always perfectly parallel. The model developed by Princen can be easily extended to describe the liquid morphology on crossed fibers (**Figure 6*c***): For small angles, the liquid spreads as a column between the fibers until d reaches d_m. If the volume exceeds the amount that can be contained in this column, an accumulation of fluid will appear as a drop at one edge. This accumulation is preferentially asymmetric, which can be explained with energetic arguments (Sauret et al. 2014). Furthermore, above a critical angle, the spacing between the fibers is such that the preferred state becomes one compact hemispherical drop centered at the node. A similar analysis can be further extended to cases involving varied interfiber distances, drop volumes, and contact angle, following the same steps as for parallel fibers (Sauret et al. 2015). When the fibers

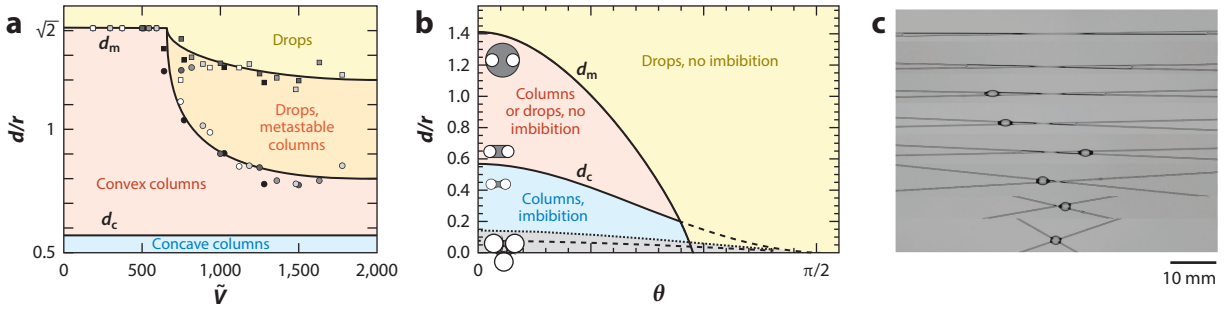

Figure 6

(*a*) Existence diagram of the different liquid morphologies between parallel cylindrical fibers as a function of distance d/r and volume volume $\tilde{V} = V/r^3$ for a contact angle of $\theta = 0$. Panel *a* adapted with permission from Protière et al. (2013). (*b*) Evolution of the maximum distance d_m and critical distance d_c with the contact angle θ. The lower dashed boundary corresponds to the region of disintegrated columns between 3 and 4 fibers. (*c*) Evolution of the liquid morphology on crossed fibers with increasing angle between fibers. Panel *c* adapted with permission from Sauret et al. (2014).

are flexible, the column shape is favored, as the capillary forces tend to align and draw the fibers together, thus reducing the interfiber distance; however, elasticity and clamped conditions may limit the deformation and, thus, the spreading, leading to morphologies similar to that of crossed fibers (Duprat et al. 2012, Sauret et al. 2017).

Finally, this model can be further developed to study the morphology of liquid in packings of three or more fibers, which are reasonable models of textile yarns (Princen 1969a,b, 1970a). Using similar arguments, one can obtain the variation of the spreading angle α for multiple cylinders (**Figure 7*a***). As the distance between fibers decreases, the liquid recedes along the fibers. Below a critical distance, the angle becomes lower than that of the two-fiber system and the liquid switches

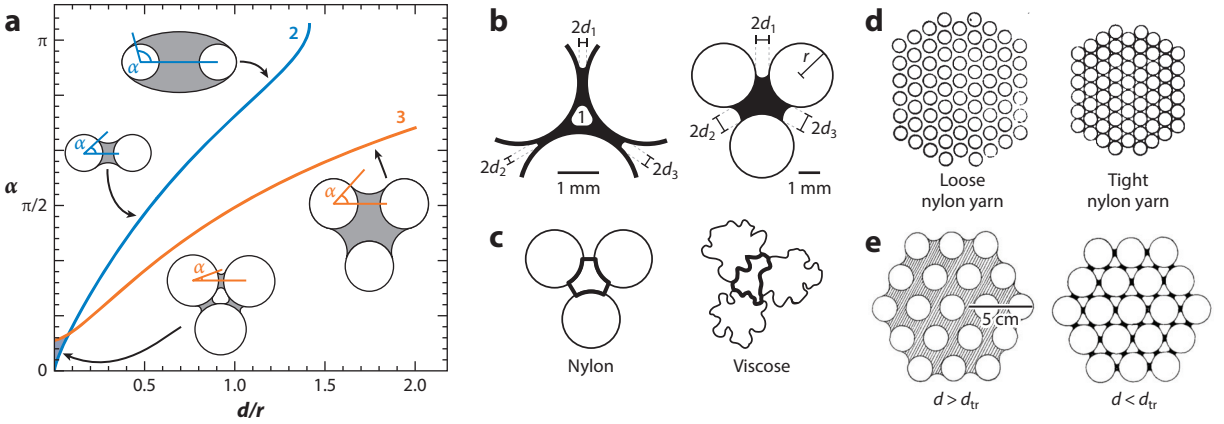

Figure 7

(*a*) Evolution of the spreading angle α as a function of the interfiber distance d/r, for two (*blue*) and three (*orange*) fibers. The shaded region in the plot represents the region in which columns are disintegrated. Insets adapted with permission from Princen (1970a). (*b*) Disintegrated and filled columns between polypropylene rods ($r = 1.5$ mm) shown with solidified epoxy resin. Panel *b* adapted with permission from Lukáš et al. (2006). (*c*,*d*) Packing of (*c*) cylindrical nylon and viscose fibers and (*d*) a loose (low-twist) and a tight (high-twist, thus more compact) yarn. Panels *c* and *d* adapted with permission from Minor et al. (1959a). (*e*) Liquid morphologies in a hexagonal packing, where the transition between filled and disintegrated columns occurs at small interfiber distances. Panel *e* adapted with permission from Princen (1970a).

to a disintegrated column, with a hole opening at the center of the pore. This was shown experimentally by Lukáš et al. (2006) by polymerizing resin drops on cylinders to obtain clean cross sections (**Figure 7*b***). While this description might fail for irregular fibers (such as viscose) for which the packing density is greatly increased (**Figure 7*c***), these considerations can help explain some observations made with loose (low-twist) or tight (high-twist) yarns, where liquid will either completely or only partially fill the interfiber channels (**Figure 7*d*,*e***).

3.3. Capillary Forces

The description of the column shape allows one to directly express the force exerted by a liquid between two adjacent fibers, which is given by the sum of the wetting force acting along the liquid surface F_w and the capillary pressure inside the column F_p, i.e.,

$$F = F_w + F_p = 2\gamma\ell\left[\sin(\alpha+\theta) + \sin\alpha\frac{r}{R}\right], \qquad 3.$$

where ℓ, α, and R/r are functions of the interfiber distance, d/r. For $d > d_c$, the pressure force is repulsive, as R is negative, and the wetting force dominates; as the interfiber distance decreases, the pressure force becomes dominant. For a given volume, the sharp increase of the force with decreasing distance is mostly due to the quick increase in wetting length ℓ, in addition to the receding angle α and decreasing radius R (**Figure 8*a***). Early measurements of the capillary force between textile fibers showed that adhesive forces were present as soon as some moisture was present; a typical order of magnitude of 3×10^{-5} N for perfectly wetted glass fibers of radius $r = 41$ μm is in agreement with the expected Laplace pressure force (Preston & Nimkar 1952). However, this simplified description fails to describe the forces observed with viscose and wool fibers, which have an irregular surface and natural crimp and may swell and soften in water (Preston & Nimkar 1952).

For larger distances $d > d_m$, the liquid adopts a drop morphology for which the length and the exerted force only slightly vary (**Figure 8*b***). The force remains almost linear with the wetted length ℓ for both drop and column shape (**Figure 8*c***), with a prefactor close to 2; i.e., the force

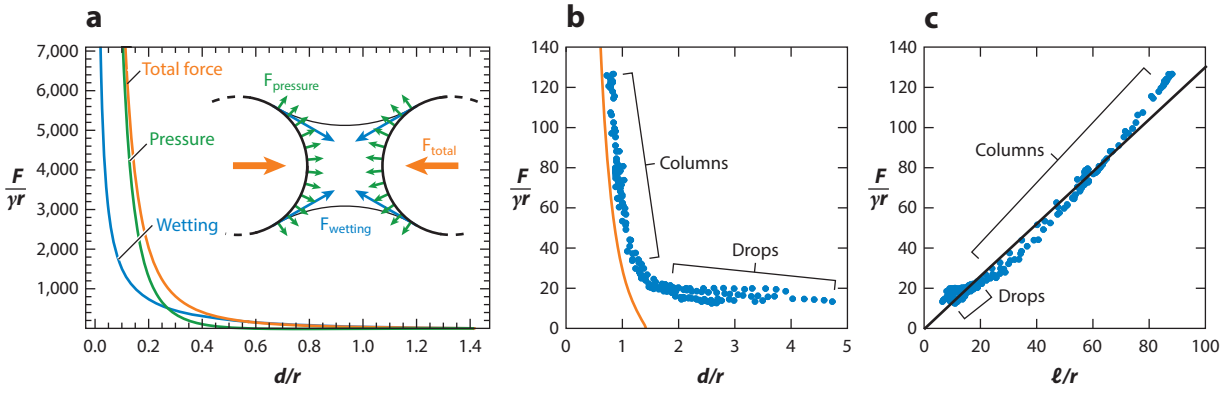

Figure 8

(*a*) Evolution of the normalized interfiber force $F/\gamma r$ exerted by a liquid column (*orange*), which is the sum of the wetting force (*blue*) and the pressure force (*green*), as a function of the interfiber distance d/r from Equation 3 for total wetting ($\theta = 0$). (*b*) Experimentally measured force of 3 μL of silicone oil ($\gamma = 21$ mN/m) deposited between two nylon fibers ($r = 0.2$ mm). Plotted data are from Duprat et al. (2020), and the orange line is from Equation 3. The discrepancy between Equation 3 and the experimental data is probably due to the end menisci that are neglected in the calculation. Close to $d = d_m$, the derived expression fails, as it predicts a force that vanishes. (*c*) The same data from panel *b* plotted against the wetted length ℓ/r. The black line is given by $F = 1.6\gamma\ell$.

always remains close to $2\gamma\ell$. The exact prefactor depends on the drop volume through the complex 3D shape of the liquid droplet, particularly the advancing edges along the fibers that provide the attractive force (**Figure 3*d***). In fact, the force exerted by drops decreases for increasing volumes, as has been noted in numerical simulations (Soleimani et al. 2015) and indirectly measured with the deflection of flexible fibers (Duprat et al. 2012); however, a complete characterization of this force is still lacking. For crossed fibers (i.e., at an intersection), the liquid exerts a torque that tends to parallelize the fibers (Preston & Nimkar 1952, Bedarkar & Wu 2009, Virozub et al. 2009, Bintein 2015).

Elastocapillarity: elastic deformations mediated by surface tension

Bending stiffness: $B = EI$, with E the Young modulus and I the second moment of area, which for cylindrical fibers is $I = \pi r^4/4$ and for thin hollow tubes of radius r and thickness e is $I = \pi r^3 e$

Elastocapillary length: the length above which flexible slender structures may be deformed by capillary forces; $\ell_{b^*} = \sqrt{\frac{EI}{2\pi r\gamma}}$ for cylinders and $\ell_{b'} = \sqrt{\frac{Ee^3}{24(1-\nu^2)\gamma}}$ for lamellae of thickness e and Poisson's ratio ν

4. ELASTOCAPILLARY DEFORMATIONS

The capillary force described in the previous section may act to locally deform fibers or pores within fibers, with consequences at the scale of the textile. The deformations induced by capillary forces fall into elastocapillary interactions [the reader is invited to consult a review on the subject of elastocapillarity by Bico et al. (2018)]. By comparing the typical capillary force $p\gamma\cos\theta$ to the force necessary to bend a slender structure B/L^2, where B is the bending stiffness, we can obtain the characteristic elastocapillary length, $\ell_b = \sqrt{EI/(p\gamma\cos\theta)}$, which can be made explicit for fibers and thin plates (Bico et al. 2018). In textiles, elastocapillary deformations are expected to occur in the pores and lumen of fibers at the micron scale, as well as between fibers at the millimeter scale.

4.1. Drying-Induced Shrinkage

When a wet textile is dried, many air–liquid interfaces appear. Those interfaces act to bring adjacent fibers together, creating large deformations, as in, for example, the apparent shrinkage of many fibrous materials upon drying. In particular, Kamo et al. (1992) have reported the evaporation-driven shrinkage of fibrous membranes after wetting/drying cycles, using different solvents. Microscopic observations reveal the collapse of adjacent fibers (**Figure 9*a***). An indirect measurement of this fiber collapse can be obtained by placing a large drop on the surface of the membrane; the global contact angle θ_{app} decreases with immersion time, revealing the pore changes of the underlying microstructure (Lv et al. 2010). During drying, the entire membrane thus shrinks, with an overall shrinkage linked to the local deformation of individual fibrils of length L: $\Delta L/L = (L_{initial} - L_{dried})/L_{initial}$. Assuming that the fibers are deformed through bending only by a punctual capillary force $F \sim 2\gamma L$ (for a fully wetted fiber in total wetting, and assuming $\alpha \sim \pi/2$), Kamo et al. (1992) estimated the typical deflection at the center of fibrils, $\delta \sim \frac{FL^3}{B} \sim \frac{\gamma L^4}{B}$, leading to an apparent shrinkage of

$$\frac{\Delta L}{L} \sim \left(\frac{\gamma L^3}{EI}\right)^2 \equiv \left(\frac{L}{\ell_b}\right)^4. \quad 4.$$

The dependence on γ^2, as well as the increase of shrinkage with increasing fiber length, is well observed in experiments (**Figure 9*b***). Furthermore, many textiles experience structural changes upon wetting–drying cycles. While many factors may influence the dimensional stability of textiles (i.e., their shrinkage upon wetting–drying cycles), including the swelling of fibers, fiber rearrangements, felting, and the release of manufacturing strains due to the softening of individual fibers and the release of fiber–fiber joints (Saville 1999), the role of capillary forces can be illustrated by the influence of the drying process on the shrinkage of fabrics. Indeed, as shown by Mikučionienė & Laureckienė (2009), tumble-dried textiles, in which capillary bridges are potentially broken by centrifugal forces, experience less shrinkage than line-dried textiles, where menisci may act locally to deform the fibers (**Figure 9*c***). Evaporation-induced fiber collapse also induces changes in

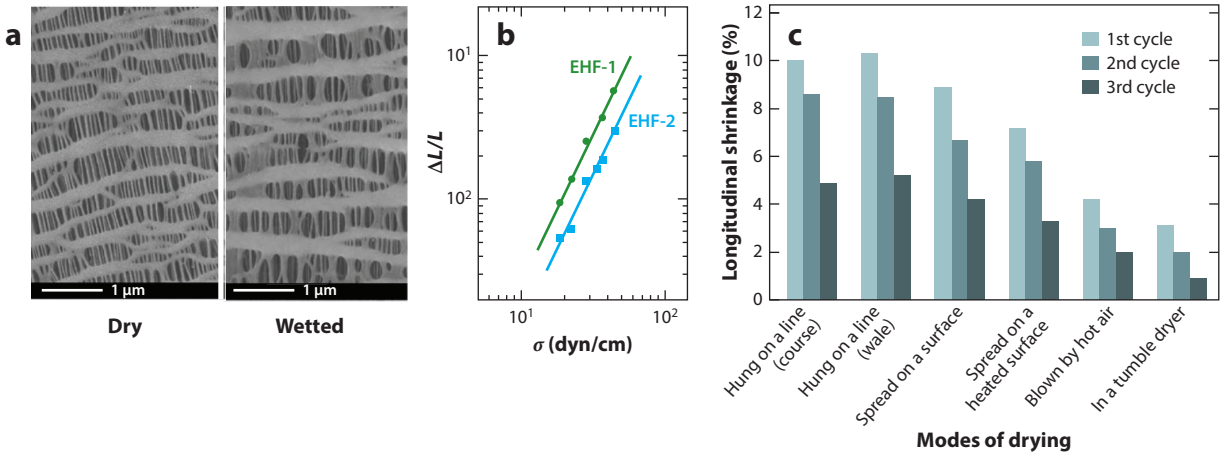

Figure 9

(*a*) A dry and wetted polypropylene hollow fiber membrane, showing the collapse between adjacent fibers. Panel *a* adapted with permission from Lv et al. (2010). (*b*) Wetting and drying of microporous polyethylene hollow fiber membrane (EHF) of initial length L_{initial} and length after wetting and drying L_{dried}. The apparent drying-induced shrinkage $\Delta L/L$ of a polypropylene membrane as a function of the surface tension σ of the solvent used for drying at 20 °C, for two membranes made of microfibrils of the same diameter but with a longer length in EHF-1 than in EHF-2. Panel *b* adapted with permission from Kamo et al. (1992). (*c*) Shrinkage of cotton knitted fabrics after several washing/drying cycles for different drying modes. Panel *c* adapted from Mikučionienė & Laureckienė (2009) (CC-BY 4.0).

permeability as the pore size is reduced, with changes, for example, in the imbibition dynamics of woven clothes (Agrawal et al. 2017) or in the air permeability of textile masks, with consequences for breathability and efficiency (DGA 2020).

4.2. Capillary Forces in Paper

The final strength of a paper sheet arises from fiber–fiber bonding and entanglement friction—i.e., from the contacts between fibers that are established during the consolidation stage as water is removed from the pulp fiber suspension by pressing and drying (van de Ven 2008, Tejado & van de Ven 2010, Schmied et al. 2013, Belle & Odermatt 2016). This process thus involves liquid–air interfaces; indeed, in the early stages of paper dewatering, capillary forces are acting to bring the fibers and fibrils closer, thus providing some of the fiber–fiber close contacts that lead to bonding and entanglements (Belle & Odermatt 2016) (see **Figure 1*a***) early in the dewatering process at $\phi = 80\%$). The fact that fibers are drawn into close molecular contact fairly early in the process is shown by the possibility of forming paper sheets even when hydrophobic sizing agents are added to the solution; these particles, which would otherwise prevent fiber–fiber adhesion, are only distributed on the fiber surfaces during the late stages of drying after bonding between fibers has already occurred (Hubbe 2014). While dry cellulosic fibers are quite stiff ($E_{\text{dry}} = 1$–10 GPa), they are greatly softened when wet ($E_{\text{wet}} \sim 10$ MPa), as they are swollen with water (Persson et al. 2013). In most of the process, the fibers are thus deformable, which is actually crucial to ensure their entanglement during consolidation; once the network is formed, and the final water is removed, the fibers stiffen. Typical values for cellulose fibers [e.g., $E_{\text{wet}}/(1-\nu^2) \sim 30$ MPa, $\nu \sim 0.4$, $r \sim 25$ µm, $e \sim 5$ µm (Persson et al. 2013)] wetted by water ($\gamma = 70$ mN/m) give elastocapillary lengths of the order of $\ell_{b^*} \sim 700$ µm, i.e., of the same order as the length of pulp fibers, which may thus collapse together as water is removed. Fibers in close contact may then form hydrogen

Permeability *k*: dimension measuring the ability of a porous material to allow fluids to pass through it; typical dimension $k \sim r_{\text{p}}^2$, with r_{p} the pore size

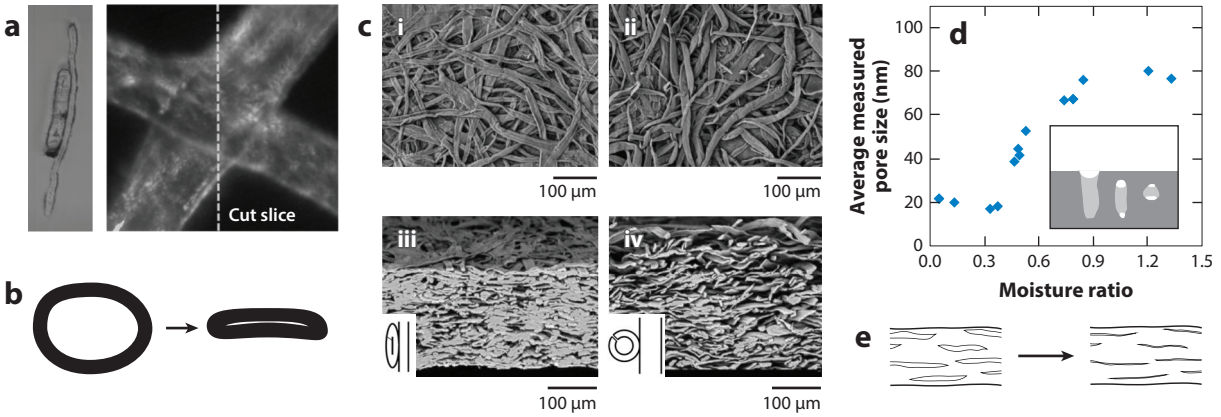

Figure 10

(*a*) Adhesion of two cellulosic fibers upon drying of a pulp suspension, showing collapsed lumens: (*right*) top view and (*left*) cross section. Panel *a* adapted with permission from Kappel et al. (2010). (*b*) Collapse of the lumen of hollow fibers upon water removal. (*c*) A sheet of paper made with different solvents: (*i*,*ii*) top views and (*iii*,*iv*) cross sections. Subpanels *i* and *iii* show water of high surface tension ($\gamma = 70$ mN/m, elastocapillary lengths for the lumen $\ell_{b'} \sim 50$ μm and for the fibers $\ell_{b^*} \sim 750$ μm), exhibiting collapsed lumens and a compact sheet. Subpanels *ii* and *iv* show ethanol with low surface tension ($\gamma = 22$ mN/m, $\ell_{b'} \sim 90$ μm, $\ell_{b^*} \sim 1{,}300$ μm), exhibiting open lumens and a less compact sheet. Panel *c* adapted with permission from Tejado et al. (2014). (*d*) Evolution of the average pore size as a function of the moisture content, showing the progressive closure of pores of decreasing size as water is removed from cellulose fibers. Panel *d* adapted with permission from Park et al. (2006). (*e*) Collapse of intrafiber pores upon drying.

bonds, leading to a strong binding (**Figure 10*a***). In this picture, we can note that the lumen of the cellulose fibers is collapsed. Indeed, as water is further removed, the capillary bridges inside the lumen may cause its deformation (**Figure 10*b***). A crude criterion may be given by comparing the radius of the hollow cellulose fibers and the elastocapillary length for thin plates $\ell_{b'}$, which is of order 50 μm for wet cellulose fibers. Reducing surface tension by replacing water with a low–surface tension solvent such as ethanol increases $\ell_{b'}$ and ℓ_{b^*}, thus preventing lumen collapse and leading to less compact paper sheets (**Figure 10*c***). Finally, in the later stages of drying, water is mostly contained in the small pores of the fiber wall; their progressive collapse as water is removed is illustrated in **Figure 10*d*,*e***. Pore closure, which may be reversible or irreversible, and structural changes during drying may be avoided by solvent exchange or freeze drying/sublimation to prevent the emergence of interfaces and thus capillary forces (Maloney et al. 1997, Park et al. 2006, Peng et al. 2012, Cichosz & Masek 2019). In beaten pulp, an additional elastocapillary effect can be observed as fine fibers mat onto larger fibers, forming a fine-scale interfiber network that is important in recycling (Hubbe et al. 2007, Belle & Odermatt 2016).

4.3. Capillary Stretching of Elastic Fibers

A simple experiment, consisting of a single slowly evaporating droplet bridging two elastic fibers clamped at both sides, reveals the main features of this evaporation-induced contact formation (**Figure 11*a***). As the drop evaporates, the fibers are deformed due to an increased capillary force, and the drop spreads. At a critical time (i.e., at a critical volume), the drop spontaneously spreads, greatly deforming (or zipping) the fibers and forming zipped columns similar to those in the membrane in **Figure 9*a***. Zipping occurs as the drop imposes a force sufficient to bring the fibers within the distance d_c at which liquid starts wicking between the fibers (Duprat & Protière 2015). Similar observations can be made for fibers that are free to bend (Duprat et al. 2013). In that case,

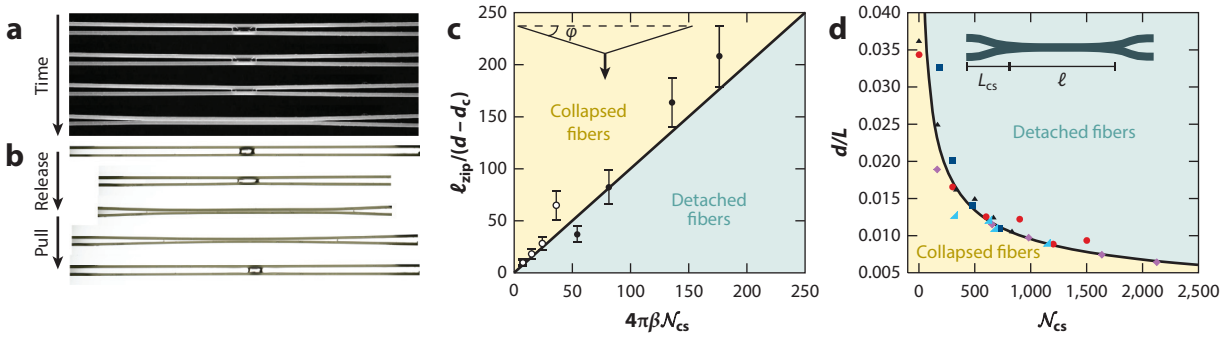

Figure 11

(*a*) Evaporation of an isopropanol drop on two elastomeric polyvinyl siloxane (PVS) fibers (of diameter $2r = 400$ μm) clamped at both ends. Time between two successive snapshots: 12.5 s. (*b*) Morphology of a small amount of liquid (paraffin oil) on flexible PVS fibers of diameter $2r = 400$ μm, length L, and Young modulus E as the strain ϵ is varied (by pulling or releasing the fibers). Similar morphologies are observed when varying the interfiber distance d. (*c*) Zipping condition [the minimal liquid length ℓ_{zip} required to induce zipping (i.e., where the interfiber distance d reaches the critical distance for spreading d_c)] and (*d*) unzipping condition (maximal deformation d/L above which collapsed fibers detach) as a function of the fiber properties $\beta = r/L$ and capillary stretching number $\mathcal{N}_{cs} = E\epsilon r/\gamma$. Panels *b*–*d* adapted with permission from Duprat & Protière (2015).

we can estimate the critical volume at which the force is sufficient to deform the fibers up to d_c from an empirical expression of the evolution of the capillary force with the drop volume (Duprat et al. 2012). It is thus possible to predict the critical volume at which the evaporation-induced zipping will occur and, in combination with the detailed kinetics of evaporation, to estimate the time at which this collapse occurs (Duprat et al. 2013). In textiles, fibers are generally constrained and may be modeled as clamped fibers under tension T. In this case, most of the deformation's energetic cost comes from stretching (i.e., bending can be neglected). Comparing tension ($T \equiv E\epsilon r^2$) and capillary forces ($F \equiv \gamma r$) introduces a capillary-stretching number $\mathcal{N}_{cs}$.

Zipping and unzipping transitions may then be obtained by varying the capillary-stretching number $\mathcal{N}_{cs}$ (for example, by controlling the tension applied to the fibers): When the tension is decreased, the drop spreads and zips the fibers, while when the tension is increased, the fibers separate (**Figure 11*b***). Zipping occurs as the drop imposes a force $F \sim 2\gamma\ell_{zip}$ sufficient to overcome the tension in the fibers, $T = E\epsilon\pi r^2$, and bring the fibers at a distance d_c, i.e., to deform the fibers with an angle $\phi \approx 2(d - d_c)/L$ such that

$$\frac{\ell_{zip}}{d - d_c} = \frac{4\pi r}{L}\mathcal{N}_{cs}, \qquad 5.$$

as shown in **Figure 11*c***. As the liquid spreads, the applied force increases, finally leading to a liquid column between two collapsed fibers. Elasticity limits the spreading, as it tends to minimize the deformation, which is confined to the deformed regions near the clamped edges [i.e., to the dry length $L_{cs} = (L - \ell)/2$]. A minimization of the total (elastic and surface tension) energy, $\mathcal{E}_{total} = \mathcal{E}_e + \mathcal{E}_\gamma \sim E\epsilon\pi r^2 \frac{d^2}{L_{cs}} - \gamma r(L - 2L_{cs})$, yields the dry length $L_{cs} \sim d\sqrt{\mathcal{N}_{cs}}$. The length L_{cs} increases linearly with the interfiber distance, providing a strong adhesion between the fibers (Duprat & Protière 2015, Duprat et al. 2020). Detachment, or unzipping, occurs when L_{cs} reaches $L/2$, i.e.,

$$\frac{d}{L} \sim \frac{1}{\sqrt{\mathcal{N}_{cs}}}, \qquad 6.$$

as shown in **Figure 11*d***. Zipping/unzipping can be achieved by decreasing/increasing d or releasing/pulling on the fibers. The changes in liquid morphology and, thus, capillary forces induced by mechanical traction/compression of this simple two-fiber system may provide some

Capillary-stretching number: $\mathcal{N}_{cs} = E\epsilon r/\gamma$ represents intrinsic material properties (size r, effective elasticity $E\epsilon$ with the prestrain ϵ, surface tension γ) and quantifies the amount of deformation that can be sustained by capillary forces

insights into some of the processes developed to minimize textile shrinkage upon wetting and drying, i.e., to improve their dimensional stability against moisture. These processes, which may be mechanical (e.g., Sanforizing, which consists in compressing and flexing the fabric during wet manufacturing), are also chemical, in particular to decrease fiber swelling. Indeed, the size changes and the softening of the fibers induced by swelling will drastically affect the shape and tensions at the scales of two fibers, of a twisted yarn, and of the textile, an effect that has yet to be investigated in model systems.

4.4. Rearrangements in Fibrous Assemblies

A simple experiment to demonstrate the importance of capillary forces in fibrous assemblies was proposed by Burgeni & Kapur (1967) and later reproduced by, e.g., Schuchard & Berg (1991). The experiment involves putting a dilute pad of fibers in contact with a liquid. When the liquid imbibes the flexible fibrous web, the surface tension forces exerted by the menisci pull the fibers together, leading to collapses and realignments; there is a spontaneous rearrangement of the fibers and a densification of the web (reduction in total volume) while it continues to take up water, as long as the web is not fully saturated. At saturation, the fiber aggregates are able to recover from the stresses imposed by the menisci. Subsequent cycles exhibit a much narrower hysteresis loop, as most fibers are already rearranged, and a faster imbibition, as fibers are aligned into better capillaries. The influence of the textile structure on wicking is the subject of the next section.

5. WICKING DYNAMICS

When a textile is placed in contact with a liquid, the liquid can spontaneously wick in between or inside the fibers; the liquid advances in the pores owing to a reduction of pressure at a curved front meniscus, or within the fiber through swelling, with imbibition and absorption rates depending on the specific materials (fiber type) and geometry (density, weave and knit pattern, yarn tension, twist, etc.). While the dynamics of liquid invasion in a textile may be modeled through pore network models relying on an accurate description of pore space, for example, obtained thanks to advanced experimental techniques such as X-ray microtomography (e.g., Faessel et al. 2005, Sun et al. 2015), these models are specific to given systems and conditions and lack generality and predictability. Efforts have been made to describe imbibition in textiles using macroscopic diffusive models (Kissa 1996, Patnaik et al. 2006). In this section, we describe these imbibition phenomena, with a particular emphasis on the consequences of the multiscale structure of textiles.

5.1. Imbibition Dynamics: Darcy's and Bell–Cameron–Lucas–Washburn's Laws

The flow through porous media is well described by Darcy's law, which relates the flow rate to the driving pressure p such that the average velocity is given by $\bar{\mathbf{u}} = -(k/\mu)\nabla p$, with k the permeability characteristic of the considered porous material and μ the fluid viscosity. In spontaneous imbibition, or wicking, the liquid can only advance if the pressure difference between the liquid in the textile (the pore pressure p_c) and in the bath (the atmospheric pressure p_0) is negative ($p_c - p_0 < 0$). The pore pressure, $p_c = p_0 - 2\gamma\cos\theta/r_p$, where r_p is the typical pore size, is given by the Laplace pressure, which gives a first condition for wicking as $\theta < \pi/2$.

In one dimension (with positive-x the direction of imbibition), the evolution of the position of the imbibition front (the meniscus) x_f is thus given by

$$\frac{\mathrm{d}x_f}{\mathrm{d}t} = -\frac{k}{\mu}\frac{\mathrm{d}p}{\mathrm{d}x}, \qquad 7.$$

where $p = p_c - \rho g x$ includes gravity. Textiles are not isotropic—the permeability differs in the warp and weft directions due to different assemblages and twists of the filaments, as well as stresses applied to the yarn during the weaving process. For example, liquid can spread faster in the warp direction than in the weft direction even if the materials are the same due to changes in geometry (interfiber spaces) induced by stresses introduced during weaving (Agrawal et al. 2017), resulting in elliptical stains, as in **Figure 1*d***. Conversely, liquid will wick faster in materials with smaller contact angles, leading to directional imbibition and complicated patterns for blended fabrics (**Figure 1*e***) (Kim et al. 2020). Multilayered textiles alternating hydrophilic and hydrophobic layers may thus be designed to promote maximum spreading, fast evaporation, and quick transverse wicking between layers (Sharabaty et al. 2008, Kandhavadivu et al. 2015). As we have seen, washing–drying cycles decrease the pore size. Agrawal et al. (2017) observed that the imbibition speed actually increases with the number of washes. Indeed, the decrease in permeability is accompanied by an increase in pore pressure; i.e., the diffusivity actually increases. One way to measure the pore pressure independently is to measure the maximum height of capillary rise against gravity. Indeed, when the bottom of a fabric is placed in contact with a liquid, the liquid will rise as long as $p - p_0 = p_c - \rho g x < 0$ and will thus stop at an equilibrium height $x = h^*$ such that $p_c = \rho g h^*$ can be directly deduced.

For a single tube of radius r_c, the permeability and the capillary pressure can be explicitly written as $k = r_c^2/8$ and $p_c = p_0 - 2\gamma \cos\theta / r_c$, respectively. It is then possible to integrate Darcy's law to obtain the evolution of the position of the imbibition front, which without gravity (i.e., when $x_f \ll h^*$) is given by

$$x_f(t) = \left(\frac{\gamma r_c \cos\theta}{2\mu} \right)^{1/2} t^{1/2}, \qquad 8.$$

which is the classical diffusive Bell–Cameron–Lucas–Washburn's law (BCLW). This law is generally used in textiles to obtain an equivalent pore radius r_c from macroscopic measurements of the imbibition front (Kissa 1996). We can define a wicking coefficient that represents the textile characteristics such that $x_f^2 = D_w t$ (Patnaik et al. 2006). The effective capillary radius r_c, which can be directly deduced from wicking experiments with the measurement of D_w or of the capillary-gravity height h^*, depends on the shape of the fibers and yarns, although its relation to geometric pore diameter is not obvious (Perwuelz et al. 2000, Kissa 1996).

The effective capillary radius r_c is generally very small [e.g., between 0.5 and 5 μm for nonwoven textiles, as reported by Zhu et al. (2008), which is much smaller than the actual pore size]. It does not represent the real physical pore size but rather represents the lack of interconnections between pores and the increased tortuosity of the liquid (especially for thin textiles since there are less pathways for the fluid across the thickness). This geometrical effect can be taken into account by replacing r_c with $\bar{r}/\xi^2$, where $\bar{r}$ is a mean radius and ξ the tortuosity (Pezron et al. 1995). Increasing the pore connectivity (e.g., with connecting weave in multilayered fabrics) increases D_w (Sharabaty et al. 2008). Porosity and tightness, and therefore D_w, change according to knit structure or yarn torsion. Indeed, increasing twist produces a more compact yarn, i.e., a reduction in interfiber spaces and an increase of tortuosity, leading to a decrease in the wicking rate (Patnaik et al. 2006, Liu et al. 2008, Sharabaty et al. 2008). When the fibers have an irregular crenulated cross section, such as with viscose fibers, D_w may be enhanced compared to cylindrical (e.g., nylon) fibers due to higher interfiber spacing in loose yarns or, on the contrary, may be reduced due to the possibility of tighter packing when applying tension and twist (Minor et al. 1959b).

Textiles are multiscale by construction; the imbibition dynamics cannot in general be completely described by a single equivalent pore size. In the following sections we separate experiments

Diffusivity: $D = \frac{k}{\mu} \frac{\partial p_c}{\partial x}$

Capillary rise: wicking vertically against gravity

Wicking coefficient: the effective diffusion coefficient $D_w = \frac{k p_c}{2\mu} = \frac{r_c \gamma \cos\theta}{2\mu}$, where r_c is the equivalent capillary radius; $\sqrt{D_w}$ is sometimes used instead

Capillary-gravity height: for a tube of radius r_c, the equilibrium height $h^* = \frac{2\gamma \cos\theta}{\rho g r_c}$ is classically termed Jurin's height, although first described by Francis Hauksbee

Porosity: the fabric density ρ_t and fiber density ρ_f are linked through the porosity, $\epsilon = 1 - \rho_t/\rho_f$

with wetting solvents, which do not penetrate fibers, that reveal the multiscale aspects of the textile structure and experiments with swelling solvents, which imbibe between and within the fibers.

5.2. Pore Distributions and Precursors of Imbibition

The presence of pores of different sizes can be demonstrated by looking at the capillary rise of a wetting liquid in a woven cotton textile (**Figure 12*a***). The position of the imbibing front does not follow BCLW. Pezron et al. (1995) showed a dual imbibition, i.e., volume imbibition within the yarn (between the fibers) and surface retention in the alveoli between yarns. These two dynamics are measured independently: The volume imbibition is measured in experiments with a sample coated with a gel such that wicking is prevented on the surface, and the surface retention is measured with an absorbent wipe (**Figure 12*b***). For a textile of height h_0, the mass absorbed by the textile is thus the sum of surface wicking in the alveoli, sensitive to gravity (here $r_c = 240$ μm and $h^* \simeq 1.5$ cm), and of the volume imbibition between yarns and filaments (here $r_c = 2.3$ μm and $h^{**} \simeq 70$ cm $\gg h_0$):

$$m_a(h_0) = \rho_l(S_v + S_s)h_0 \quad \text{if } h_0 < h^*, \tag{9.}$$

$$m_a(h_0) = \rho_l(S_v h_0 + S_s h^*) \quad \text{if } h_0 > h^*, \tag{10.}$$

where S_v and S_s are geometrical parameters deduced from the experiments (**Figure 12*c***). Here the two processes are independent since both timescales are similar, and there are no exchanges between surface and volume; a different dynamics could occur if the filling times were different (e.g., a tight structure and large alveoli). This dual-scale dynamics can be further seen using neutron imaging of woven and jersey knit fabrics (**Figure 12*d***) (Parada et al. 2017). The resulting measurement of the moisture distribution reveals that the intrayarn wicking reaches the top of

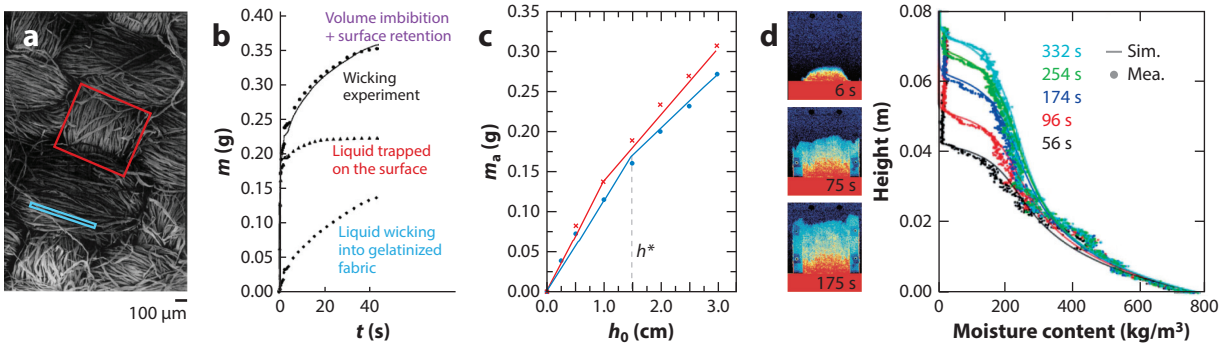

Figure 12

(*a*) Scanning electron microscopy image of a cotton woven fabric, where the liquid can imbibe between the filaments of the yarn (*blue*) and on the surface in the alveoli formed by the woven structure (*red*). (*b*) Evolution with time of (*circles*) the mass m of liquid uptake as the bottom of the woven fabric is put in contact with a bath of liquid; (*diamonds*) the mass m_v of the liquid wicking in the same fabric but coated with a gel, thus preventing any wetting on the surface; (*triangles*) the mass m_s of the liquid trapped in the alveoli measured by absorbing the liquid present at the surface with a very permeable wipe; and (*black line*) the sum of $m_v + m_s$. (*c*) The total absorbed mass m_a as a function of the fabric height for two liquids. The lines are given by Equations 9 and 10. Panels *a–c* adapted with permission from Pezron et al. (1995). (*d*, *left*) Evolution of the moisture profile during capillary rise in a cotton knit, exhibiting a region of low moisture content (*blue*) where only the yarn pore space (between filaments) is filled, and a region with higher moisture content (*yellow-red*) where both yarn and void pore spaces are filled. (*Right*) Corresponding moisture profiles along the fabric height at different times, modeled as a dual-pore system. Panel *d* adapted with permission from Parada et al. (2019b). Abbreviations: Mea., measurement; Sim., simulation.

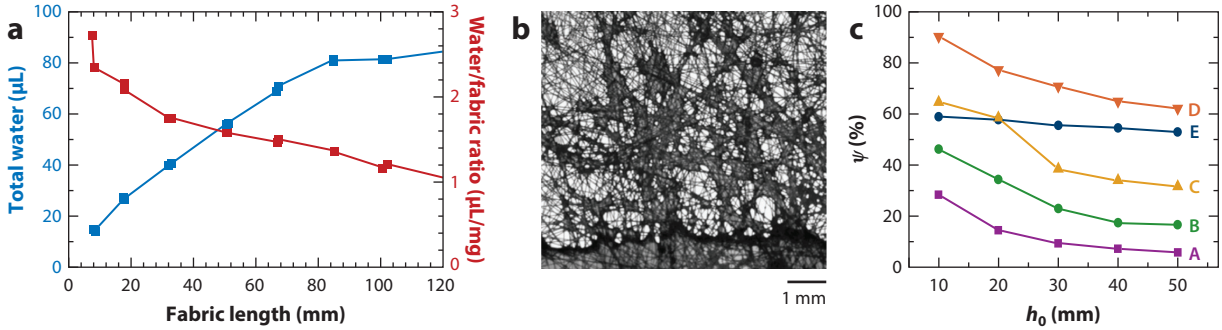

Figure 13

(*a*) Water retention in a cotton fabric as a function of the fabric length, showing the total water retention (*blue squares*; *left axis*) and the water-to-fabric weight ratio, i.e., saturation ψ (*red squares*; *right axis*). Panel *a* adapted with permission from Hsieh et al. (1992). (*b*) Imbibition of a totally wetting liquid (colored decane; $\gamma = 23.6$ mN/m, $\mu = 0.91$ mPa·s) by a nonwoven fabric made of polyester fibers with PBT (polybutylene terephthalate) thermobonding fibers (basis weight 10 g/m^2, thickness 111 μm, and porosity 79.8%). We clearly see that the nonwoven fabric is not homogeneously saturated. (*c*) The corresponding saturation level ψ as a function of the fabric sample height h_0 for different nonwoven fabrics imbibed with decane. The fabric depicted in panel *b* is labeled B. Panels *b* and *c* adapted with permission from Zhu et al. (2008).

the sample while the interyarn pore wicking quickly reaches its maximum height (about 2 cm). As a result, there is an unsaturated region where the textile is only partially filled with liquid ahead of the sharp wetting front close to the reservoir, below which both structures are filled with liquid.

This saturation gradient is often observed in textiles. By measuring the total water retention m_w/m_f after capillary rise for samples of the same fabric with different heights, Hsieh et al. (1992) showed a decrease of saturation away from the liquid source (**Figure 13*a***). Interestingly, a gradient of saturation is also observed in nonwoven fabrics, as shown by Zhu et al. (2008) (**Figure 13*b***). The saturation level ψ, which decreases along the fabric's height, also decreases with increasing porosity (**Figure 13*c***). The saturation never reaches 100%, as some pores remain unfilled, especially in thin nonwoven fabrics where pore connectivity is low.

Cryo-SEM (scanning electron microscopy) images of imbibing paper reveal that, ahead of fully filled pores, the liquid is transported in films along fibers (**Figures 1*b*** and **14*a***). There are thus two macroscopic fronts: The main front saturates the medium, and a thinner, precursor front propagates ahead faster than the main front using a finer structure of the fibrous media, for example, as films along fibers. de Azevedo et al. (2008) visualized these two fronts using magnetic resonance imaging to obtain the moisture profile ψ along the imbibition direction (**Figure 14*b***). The moisture profiles exhibit a flat precursor front followed by an extended unsaturated region that are of similar shape to those seen in the cotton knits (**Figure 12*d***). The profiles collapse onto a universal curve when plotted against the variable $\xi = x/t^a$, which is captured by introducing a moisture- and time-dependent transport diffusivity of the form $D(\psi, t) \propto t^{2a-1}\delta(\psi)$, where the exponent a depends on the sample properties (de Azevedo et al. 2008). To investigate precursor fronts, Bico & Quéré (2003) proposed a model bidisperse experiment by placing a thin fiber (of radius $r_1 = 170$ μm) in a larger tube (radius $r_2 = 600$ μm). The liquid can wick in the tube and in the interstice between the fiber and the tube; there are, thus, two wetting fronts (**Figure 14*c***). In this situation, both fronts are diffusive (**Figure 14*d***). If the two pores were not connected, the liquid would wick more slowly in the smaller one (along the fiber) according to Equation 8. However, when the pores are connected, the liquid in the small interstice can pump liquid out of the large pore due to a higher pore pressure ($p_c \propto \gamma/r_1$) while minimizing the viscous friction ($k/\mu \propto r_2^2/\mu$)

Saturation level ψ: the volume of pores filled with liquid divided by the total pore volume; ψ is obtained with either local concentration or mass measurements

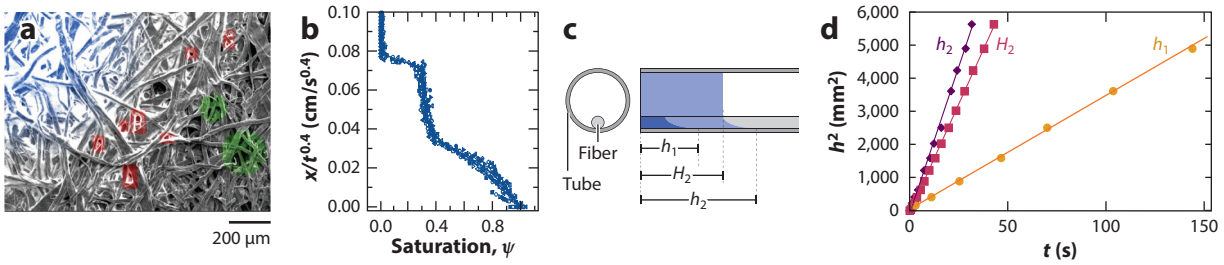

Figure 14

(*a*) Cryo-scanning electron microscopy image of an imbibition front in paper, exhibiting a fully saturated zone (*blue*), partially filled pores (*red*), and films along fibers (*green*). Panel *a* adapted with permission from Roberts et al. (2003). (*b*) Self-similar moisture profiles during the imbibition of a cylinder filled with cellulose fibers by water, obtained with magnetic resonance imaging. Panel *b* adapted with permission from de Azevedo et al. (2008). (*c*) A model bidisperse system consisting of a horizontal tube containing a thin fiber. (*d*) Results corresponding to the model system in panel *c*, showing the time evolution of the height of a totally wetting silicone oil (viscosity μ and surface tension γ) along the fiber alone (h_1), in the connected bidisperse system along the fiber (h_2), and in the tube (H_2). For each case, we can define a wicking coefficient D_w such that $h^2 = D_w t$ and an equivalent pore radius $r_c = 2\mu D_w/\gamma$, which gives $D_{w,h_1} = 34$ mm^2/s (i.e., $r_{c,h_1} = 53$ µm), $D_{w,h_2} = 177$ mm^2/s (i.e., $r_{c,h_2} = 275$ µm), and $D_{w,H_2} = 137$ mm^2/s (i.e., $r_{c,H_2} = 213$ µm). The equivalent radius deduced from the experiment with the connected pores is higher than the equivalent radius of the individual pores. Panels *c* and *d* adapted with permission from Bico & Quéré (2003).

and is thus ahead of the front in the tube. In fact, for $r_1 \ll r_2$, the wicking coefficient of the precursor front should scale as $D_{w,h_2} \approx D_{w,H_2} + 2D_{w,h_1}$. This also highlights the tricky link between the effective capillary radius and the pore distribution, in particular when the system contains pores of different sizes that are interconnected.

Large pore size heterogeneities can be seen in the imbibition of single yarns, as shown by Perwuelz et al. (2001); the large unsaturated zone ahead of the main front is the signature of the distribution of pore sizes (**Figure 15*a***). These observations can again be reinforced with neutron

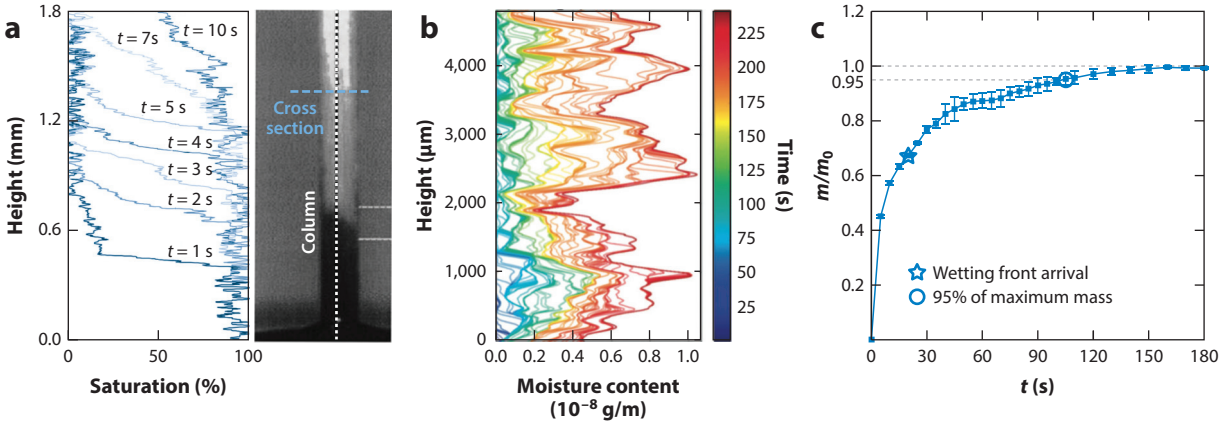

Figure 15

(*a*) Saturation profiles during imbibition of a polyester (PET) yarn with dyed PEG-400 (polyethylene glycol 400; contact angle $\theta = 20°$) at different imbibition times, where the concentration is obtained from the gray level shown in the photo (*right*). Panel *a* adapted with permission from Perwuelz et al. (2001). (*b*) Moisture profiles during imbibition of a PET yarn at different times (*color scale*) obtained from neutron imaging. Panel *b* adapted with permission from Parada et al. (2019a). (*c*) Evolution of the liquid distribution $\psi = m/m_0$ of silicone oil imbibing a piece of paper (Whatman grade 5). The moment at which the liquid front reaches the strip end is noted with a star symbol. Panel *c* adapted with permission from Chang et al. (2018).

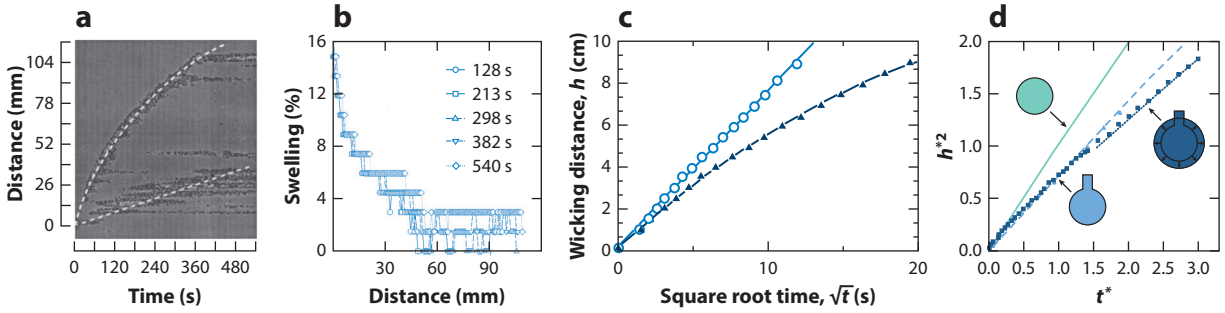

Figure 16

(*a*,*b*) Imbibition of a plug of entangled wood fibers with water: (*a*) advancing imbibition fronts as a function of time, evaluated from the gradient of the concentration distribution obtained with nuclear magnetic resonance imaging, and (*b*) the amount of swelling, measured from the dimensional change of the wet fiber matrix relative to the original dry fiber plug. Panels *a* and *b* adapted with permission from Takahashi et al. (1997). (*c*) Wicking distance h as a function of time $\sqrt{t}$ during imbibition of *n*-octane (*open circles*), which exhibits no swelling, and water (*filled triangles*), which exhibits swelling, in a composite paper strip (33% carboxymethyl cellulose, 67% cellulose). Panel *c* adapted with permission from Schuchard & Berg (1991). (*d*) Evolution of the square of the wicking distance h^{*2} as a function of time t^* for silicone oil (*triangles*, *dashed line*), which exhibits no swelling but does exhibit intrafiber pore filling, modeled as a tube connected to a slit, and for water (*squares*, *dotted line*), which exhibits swelling and intrafiber pore filling, modeled with a slit and an increase in tube radius. Time is normalized by the time to fill the intrafiber pores t_c, and wicking distance is normalized by $\sqrt{D_w t_c}$, where D_w is the wicking coefficient such that $h^2 = D_w t$. The solid green line shows Bell–Cameron–Lucas–Washburn's law, $h^{*2} = t^*$. Data taken from Chang et al. (2018) (*triangles*) and Chang & Kim (2020) (*squares*).

imaging (**Figure 15*b***): Capillary rise within the yarn consists of a fast flow along the yarn that reaches the top early but leaves the yarn unsaturated (i.e., films or corner flows along fibers), followed by a slower filling of pore spaces between filaments. Sudden jumps in moisture content correspond to the sudden filling of large pores, reflecting the large heterogeneities along the yarn length, which are greatly influenced by yarn torsion (Perwuelz et al. 2001, Parada et al. 2019a). Similarly, imbibition of oil in paper reveals a dual pore dynamics with two distinct times (Chang et al. 2018): a first filling of the interfiber pores that make up the main visible wetting front, followed by a slower diffusion through the intrafiber pores of the cellulose fibers. This dynamics can be shown by following both the mass and the wetting front (**Figure 15*c***): Once the wetting front has reached the end of the sample, the region behind continues to imbibe liquid. The front does not follow BCLW; the main front slows down, which can be well modeled by considering a tube connected to a slit. The sizes of the tube/slit depend on the interfiber-to-intrafiber pore ratio (**Figure 16*d***). Alternatively, one can add a sink term to Darcy's law to account for flow toward the fibers (Masoodi & Pillai 2010).

5.3. Swelling

The imbibing liquid might also penetrate the fibers; in fact, water swells many of the materials used in textiles (e.g., natural fibers such as cotton, cellulose, viscose, flax), and deviations from BCLW are generally observed (Pucci et al. 2016, Testoni et al. 2018). By following the imbibition of a plug made of nonwoven wood pulp fibers with nuclear magnetic resonance imaging, Takahashi et al. (1997) identified a relatively sharp imbibition front followed by a front lagging behind and corresponding to liquid diffusion inside the fibers (**Figure 16*a***). This diffusion is accompanied by swelling, i.e., matrix expansion (**Figure 16*b***). Swelling of the fibers can actually have two opposite effects. The reduction of the frictional force between fibers, the softening of the fibers, and, thus, the release of fabrication bending stresses lead to an increase of volume for an unconstrained

fibrous assembly such as a paper sheet—and, thus, an increase in thickness and in pore diameter (Steiger & Kapur 1972, Skelton 1975, Chang & Kim 2020). On the contrary, a tightly woven fabric becomes denser as the fibers attempt to swell against restraining forces, and fiber swelling occurs primarily at the expense of the interfiber space, resulting in a decrease in pore diameter (Steiger & Kapur 1972, Skelton 1975, Schuchard & Berg 1991). In the case of decreased pore diameter, Schuchard & Berg (1991) measured the imbibition of a composite paper strip and observed a deviation from BCLW (**Figure 16*c***). To take into account the changes in pore size, although neglecting the flux of liquid into the fiber walls, Schuchard & Berg (1991) introduced two radii: (*a*) the initial pore radius r_0, which is ahead of the imbibition front and thus unaffected by swelling, that sets the capillary pressure and (*b*) an effective hydraulic radius $r_h < r_0$ within the saturated fibrous network that sets the viscous friction and evolves with the swelling rate λ such that $r_h = r_0 - \lambda t$. Using these two radii in BCLW allows one to reproduce the observed dynamics. Conversely, when swelling leads to an opening of the structure, Chang & Kim (2020) also observed a deviation from BCLW (**Figure 16*d***). They took into account both the intrafiber pore diffusion, with a timescale t_c, and the expanding radius due to swelling, with a timescale t_s. Their model captures well the case of paper imbibed with water such that $t_s < t_c$, i.e., where the tube swelling near the channel entrance ends before the water suction in the slit is completed. The pore opening dynamics actually exhibits a similar deviation from BCLW as the pore restriction. Finally, imbibition has been observed to be faster in blended PET/cotton fabrics than in 100% cotton fabrics, as the presence of nonswelling PET prevents some of the swelling-induced reduction of pore size (Sharabaty et al. 2008, Achour et al. 2015). In addition, the presence of film flows may have a great impact when considering swelling fibers; indeed, modifying the liquid distribution will impact not only which regions swell or deform but also the absorption time. Recent experiments on cotton fabrics showed that while an ink droplet spreading between the filaments of a yarn (as a liquid column; **Figure 1*c***) is absorbed in less than 1 ms, the absorption time of the same drop on a single fiber is 1.6 s, which is 5,000 times faster (Zhang et al. 2020); the absorption time is actually greatly increased due to local saturation below the drop (Van de Velde et al. 2021). Furthermore, the imbibition dynamics is greatly affected by the pore shape, which might not be circular and can evolve in time due to swelling or elastocapillary effects. Deviations from the diffusive BCLW are indeed observed for conical pores (Reyssat et al. 2008) or elastic pores that change their geometry due to elastocapillary deformation (Aristoff et al. 2011, Duprat et al. 2011). In general, there is a need for multiphysics imbibition models that account for deformation and swelling in soft porous materials (Ha & Kim 2020).

SUMMARY POINTS

1. In fibrous assemblies, liquid can adopt different morphologies, from drops between separated fibers or at intersections of fibers to columns between close fibers, and may fully or partially fill the interfiber spaces.
2. With these interfaces are associated capillary forces that act to deform and eventually collapse intrafiber pores or adjacent fibers, resulting in changes in the shape or strength of textiles.
3. Liquid imbibition can occur in large-scale interyarn or interfiber pores, in finer intrayarn or intrafiber pores, in film flows along fibers, and as swelling inside fibers. These mechanisms are associated with different timescales that depend on the materials and structure of the textile, leading to a wide variety of dynamics.

FUTURE ISSUES

1. It is necessary to include swelling in elastocapillary models, including both changes in geometry and softening of the fibers.
2. The mechanical properties of textiles depend on many parameters, including the network geometry, individual fiber elasticity, friction and joint properties, and the formation and breaking of contacts, many of which may be influenced by moisture. In particular, the interactions between liquid and fibers drastically affect the mechanical behaviors of textiles (e.g., the increase of yarns' tenacity in wet conditions, swelling-induced softening, loosening of interfiber bonds), but links have yet to be made between large-scale mechanical properties and the liquid distribution, elastocapillarity, and swelling effects at the scale of a few fibers.
3. Conversely, the changes induced by moisture absorption can be harnessed to initiate large-scale motions in multilayer materials made of fibers with different orientations and arrangements, which is the basis of the hygroscopic movements of several plants. A better description of the mechanisms at play in moisture absorption at the fiber scale could help inform the design of such materials.

DISCLOSURE STATEMENT

The author is not aware of any biases that might be perceived as affecting the objectivity of this review.

ACKNOWLEDGMENTS

I thank all the students and colleagues with whom I have exchanged on this subject, in particular, Suzie Protière and Anne Perwuelz. I acknowledge Hugues Lepic and the Fondation de l'École polytechnique for funding through the Chaire professorale Jean Marjoulet.

LITERATURE CITED

Achour NS, Hamdaoui M, Nasrallah SB, Perwuelz A. 2015. Investigation of moisture management properties of cotton and blended knitted fabrics. *Int. J. Mater. Metall. Eng.* 9(7):891–95

Agrawal P, Barnet L, Attinger D. 2017. Bloodstains on woven fabric: simulations and experiments for quantifying the uncertainty on the impact and directional angles. *Forensic Sci. Int.* 278:240–52

Alava M, Niskanen K. 2006. The physics of paper. *Rep. Prog. Phys.* 69(3):669–723

Aristoff JM, Duprat C, Stone HA. 2011. Elastocapillary imbibition. *Int. J. Non-Linear Mech.* 46(4):648–56

Balankin AS, Morales D, Susarrey O, Samayoa D, Trinidad JM, et al. 2006. Self-similar roughening of drying wet paper. *Phys. Rev. E* 73(6):065105

Bedarkar A, Wu XF. 2009. Capillary torque in a liquid bridge between two angled filaments. *J. Appl. Phys.* 106(11):113527

Bedarkar A, Wu XF, Vaynberg A. 2010. Wetting of liquid droplets on two parallel filaments. *Appl. Surf. Sci.* 256(23):7260–64

Belle J, Odermatt J. 2016. Initial wet web strength of paper. *Cellulose* 23(4):2249–72

Bico J, Quéré D. 2003. Precursors of impregnation. *Europhys. Lett.* 61(3):348–53

Bico J, Reyssat E, Roman B. 2018. Elastocapillarity: when surface tension deforms elastic solids. *Annu. Rev. Fluid Mech.* 50:629–59

Bintein PB. 2015. *Dynamiques de gouttes funambules: applications à la fabrication de laine de verre*. PhD Thesis, Sorbonne Université, Paris

Bosco E, Peerlings R, Lomans B, van der Sman C, Geers M. 2018. On the role of moisture in triggering out-of-plane displacement in paper: from the network level to the macroscopic scale. *Int. J. Solids Struct.* 154:66–77

Burgeni AA, Kapur C. 1967. Capillary sorption equilibria in fiber masses. *Text. Res. J.* 37:356–66

Chang S, Kim W. 2020. Dynamics of water imbibition through paper with swelling. *J. Fluid Mech.* 892:A39

Chang S, Seo J, Hong S, Lee DG, Kim W. 2018. Dynamics of liquid imbibition through paper with intra-fiber pores. *J. Fluid Mech.* 845:36–50

Cichosz S, Masek A. 2019. Cellulose structure and property changes indicated via wetting-drying cycles. *Polym. Degrad. Stab.* 167:33–43

Das A, Ishtiaque S, Singh S, Meena H. 2009. Tensile characteristics of yarns in wet condition. *Indian J. Fibre Text. Res.* 34(4):338–44

de Azevedo EN, Alme LR, Engelsberg M, Fossum JO, Dommersnes P. 2008. Fluid imbibition in paper fibers: precursor front. *Phys. Rev. E* 78(6):066317

de Castro TC, Carr DJ, Taylor MC, Kieser JA, Duncan W. 2016. Drip bloodstain appearance on inclined apparel fabrics: effect of prior-laundering, fibre content and fabric structure. *Forensic Sci. Int.* 266:488–501

DGA (Dir. Gén. Armement). 2020. *Lettre n° 4 à l'attention des industriels sollicitant DGA Maîtrise NRBC pour les masques*. Tech. Guid., DGA Maîtrise NRBC, Vert-le-Petit, Fr., Apr. 3

Duprat C, Aristoff JM, Stone HA. 2011. Dynamics of elastocapillary rise. *J. Fluid Mech.* 679:641–54

Duprat C, Bick AD, Warren PB, Stone HA. 2013. Evaporation of drops on two parallel fibers: influence of the liquid morphology and fiber elasticity. *Langmuir* 29(25):7857–63

Duprat C, Noûs C, Protière S. 2020. Controlling wet adhesion with elasticity. *Soft Matter* 16(28):6463–67

Duprat C, Protière S. 2015. Capillary stretching of fibers. *Europhys. Lett.* 111(5):56006

Duprat C, Protière S, Beebe AY, Stone HA. 2012. Wetting of flexible fibre arrays. *Nature* 482(7386):510–13

Durville D, Ganghoffer JF, Lomov S, Orgéas L, Kyriakides S. 2018. Multiscale modelling of fibrous and textile materials. *Int. J. Solids Struct.* 154:1–17

Dyba RV, Miller B. 1969. Evaluation of wettability from capillary rise between filaments. *Text. Res. J.* 39(10):962–70

Faessel M, Delisée C, Bos F, Castéra P. 2005. 3D modelling of random cellulosic fibrous networks based on X-ray tomography and image analysis. *Compos. Sci. Technol.* 65(13):1931–40

Gager V, Le Duigou A, Bourmaud A, Pierre F, Behlouli K, Baley C. 2019. Understanding the effect of moisture variation on the hygromechanical properties of porosity-controlled nonwoven biocomposites. *Polym. Test.* 78:105944

Gottlieb IM, Wakeham H, Virgin HM. 1958. Compressional and absorptive behavior of bulk fibre systems. *Text. Res. J.* 28:41–46

Ha J, Kim HY. 2020. Capillarity in soft porous solids. *Annu. Rev. Fluid Mech.* 52:263–84

Hearne E, Nossar M. 1983. Behavior of loose fibrous beds during centrifuging: part III: location, shape, and size of droplets of surface moisture. *Text. Res. J.* 53:236–52

Hsieh YL, Bangling Y, Hartzell MM. 1992. Liquid wetting, transport, and retention properties of fibrous assemblies. *Text. Res. J.* 62:697–704

Hubbe MA. 2014. Puzzling aspects of the hydrophobic sizing of paper and its inter-fiber bonding ability. *BioResources* 9(4):5782–83

Hubbe MA, Venditti RA, Rojas OJ. 2007. What happens to cellulosic fibres during papermaking and recycling? A review. *BioResources* 2:739–88

Kamo J, Hirai T, Kamada K. 1992. Solvent-induced morphological change of microporous hollow fiber membranes. *J. Membr. Sci.* 70(2–3):217–24

Kandhavadivu P, Rathinamoorthy R, Surjit R. 2015. Moisture and thermal management properties of woven and knitted tri-layer fabrics. *Indian J. Fibre Text. Res.* 40:243–49

Kappel L, Hirn U, Gilli E, Austria W, Schennach R. 2010. Revisiting polarized light microscopy for fiber-fiber bond area measurement—part I: theoretical fundamentals. *Nordic Pulp Paper Res. J.* 25(1):65–70

Kim HS, Michielsen S, DenHartog E. 2020. New wicking measurement system to mimic human sweating phenomena with continuous microfluidic flow. *J. Mater. Sci.* 55(18):7816–32
Kissa E. 1996. Wetting and wicking. *Text. Res. J.* 66(10):660–68
Labbé R, Duprat C. 2019. Capturing aerosol droplets with fibers. *Soft Matter* 15(35):6946–51
Liu T, Choi K-F, Li Y. 2008. Wicking in twisted yarns. *J. Colloid Interface Sci.* 318(1):134–39
Lukáš D, Chaloupek J, Košťáková E, Pan N, Martinková I. 2006. Morphological transitions of capillary rise in a bundle of two and three solid parallel cylinders. *Physica A* 371(2):226–48
Lv Y, Yu X, Tu ST, Yan J, Dahlquist E. 2010. Wetting of polypropylene hollow fiber membrane contactors. *J. Membr. Sci.* 362(1–2):444–52
Maloney TC, Li T, Weise U, Paulapuro H. 1997. Intra-and inter-fibre pore closure in wet pressing. *Appita J.* 50(4):301–6
Masoodi R, Pillai KM. 2010. Darcy's law-based model for wicking in paper-like swelling porous media. *AIChE J.* 56(9):2257–67
Mead-Hunter R, King AJ, Mullins BJ. 2014. Aerosol-mist coalescing filters—a review. *Sep. Purif. Technol.* 133:484–506
Melki S, Biguenet F, Dupuis D. 2019. Hydrophobic properties of textile materials: robustness of hydrophobicity. *J. Text. Inst.* 110(8):1221–28
Mikučionienė D, Laureckienė G. 2009. The influence of drying conditions on dimensional stability of cotton weft knitted fabrics. *Mater. Sci.* 15(1):64–68
Miller B, Coe AB, Ramachandran P. 1967. Liquid rise between filaments in a V-configuration. *Text. Res. J.* 37(11):919–24
Minor FW, Schwartz AM, Wulkow E, Buckles LC. 1959a. The migration of liquids in textile assemblies: part II: the wicking of liquids in yarns. *Text. Res. J.* 29(12):931–39
Minor FW, Schwartz AM, Wulkow E, Buckles LC.1959b. The migration of liquids in textile assemblies: part III: the behavior of liquids on single textile fibers. *Text. Res. J.* 29(12):940–49
Morton WE, Hearle JWS. 2008. *Physical Properties of Textile Fibres*. Boca Raton, FL: CRC. 4th ed.
Mullins BJ, Agranovski IE, Braddock RD, Ho CM. 2004. Effect of fiber orientation on fiber wetting processes. *J. Colloid Interface Sci.* 269(2):449–58
Ostlund S. 2018. Three-dimensional deformation and damage mechanisms in forming of advanced structures in paper. In *Advances in Pulp and Paper Research: Transactions of the 16th Fundamental Research Symposium Held in Oxford*, ed. W Batchelor, D Söderberg, pp. 489–594. Lancashire, UK: Pulp Paper Fundam. Res. Soc.
Parada MYI, Schlepütz CM, Rossi RM, Derome D, Carmeliet J. 2019a. Two-stage wicking of yarns at the fiber scale investigated by synchrotron X-ray phase-contrast fast tomography. *Text. Res. J.* 89:4967–79
Parada MYI, Vontobel P, Rossi RM, Derome D, Carmeliet J. 2017. Dynamic wicking process in textiles. *Transp. Porous Media* 119(3):611–32
Parada MYI, Zhou X, Derome D, Rossi RM, Carmeliet J. 2019b. Modeling wicking in textiles using the dual porosity approach. *Text. Res. J.* 89:3519–28
Park S, Venditti R, Jameel H, Pawlak J. 2006. Changes in pore size distribution during the drying of cellulose fibers as measured by differential scanning calorimetry. *Carbohydr. Polym.* 66(1):97–103
Patnaik A, Rengasamy RS, Kothari VK, Ghosh A. 2006. Wetting and wicking in fibrous materials. *Text. Prog.* 38(1):1–105
Peng Y, Gardner DJ, Han Y. 2012. Drying cellulose nanofibrils: in search of a suitable method. *Cellulose* 19:91–102
Persson BNJ, Ganser C, Schmied F, Teichert C, Schennach R, et al. 2013. Adhesion of cellulose fibers in paper. *J. Phys. Condens. Matter* 25(4):045002
Perwuelz A, Casetta M, Caze C. 2001. Liquid organisation during capillary rise in yarns—influence of yarn torsion. *Polym. Test.* 20(5):553–61
Perwuelz A, Mondon P, Caze C. 2000. Experimental study of capillary flow in yarns. *Text. Res. J.* 70(4):333–39
Pezron I, Bourgain G, Quéré D. 1995. Imbibition in a fabric. *J. Colloid Interface Sci.* 173:319–27
Preston JM, Nimkar MV. 1952. Capillary phenomena in assemblies of fibres. *J. Text. Inst. Trans.* 43(8):T402–22
Preston JM, Nimkar MV, Gundavda SP. 1951. Capillary and imbibed water in assemblies of moist fibres. *J. Text. Inst. Trans.* 42(2):T79–90

Princen HM. 1969a. Capillary phenomena in assemblies of parallel cylinders: I. Capillary rise between two cylinders. *J. Colloid Interface Sci.* 30:69–75

Princen HM. 1969b. Capillary phenomena in assemblies of parallel cylinders: II. Capillary rise in systems with more than two cylinders. *J. Colloid Interface Sci.* 30:359–71

Princen HM. 1970a. Capillary phenomena in assemblies of parallel cylinders: III. Liquid columns between horizontal parallel cylinders. *J. Colloid Interface Sci.* 34:171–84

Princen HM. 1970b. Contact angles from capillary rise between filaments in a V-configuration. *Text. Res. J.* 40:1069–72

Protière S, Duprat C, Stone HA. 2013. Wetting on two parallel fibers: drop to column transitions. *Soft Matter* 9(1):271–76

Pucci MF, Liotier PJ, Drapier S. 2016. Capillary wicking in flax fabrics—effects of swelling in water. *Colloids Surf. A* 498:176–84

Py C, Bastien R, Bico J, Roman B, Boudaoud A. 2007. 3D aggregation of wet fibers. *Europhys. Lett.* 77(4):44005

Reyssat M, Courbin L, Reyssat E, Stone HA. 2008. Imbibition in geometries with axial variations. *J. Fluid Mech.* 615:335–44

Roberts RJ, Senden TJ, Knackstedt MA, Lyne MB. 2003. Spreading of aqueous liquids in unsized papers is by film flow. *J. Pulp Paper Sci.* 29(4):123–31

Salehi Rad A, Hosseini Varkiyani S, Haghighat Kish M. 2013. Water retention in hollow fibres nonwoven mat. *J. Text. Inst.* 104(9):994–1002

Sauret A, Bick AD, Duprat C, Stone HA. 2014. Wetting of crossed fibers: multiple steady states and symmetry breaking. *Europhys. Lett.* 105(5):56006

Sauret A, Boulogne F, Soh B, Dressaire E, Stone HA. 2015. Wetting morphologies on randomly oriented fibers. *Eur. Phys. J. E* 38(6):62

Sauret A, Boulogne F, Somszor K, Dressaire E, Stone HA. 2017. Drop morphologies on flexible fibers: influence of elastocapillary effects. *Soft Matter* 13(1):134–40

Saville BP. 1999. *Physical Testing of Textiles*. Cambridge, UK: Woodhead

Schmied FJ, Teichert C, Kappel L, Hirn U, Bauer W, Schennach R. 2013. What holds paper together: nanometre scale exploration of bonding between paper fibres. *Sci. Rep.* 3(1):2432

Schuchard DR, Berg JC. 1991. Liquid transport in composite cellulose—superabsorbent fiber networks. *Wood Fiber Sci.* 23(3):342–57

Sharabaty T, Biguenet F, Dupuis D, Viallier P. 2008. Investigation on moisture transport through polyester/cotton fabrics. *Indian J. Fibre Text. Res.* 33:419–25

Skelton J. 1975. Interfiber forces during wetting and drying. *Science* 190(4209):15–20

Soleimani M, Hill RJ, van de Ven TGM. 2015. Capillary force between flexible filaments. *Langmuir* 31(30):8328–34

Steiger FH, Kapur C. 1972. The absorption of liquids by compressed fiber systems. *Text. Res. J.* 42(8):443–49

Sun Y, Kharaghani A, Metzger T, Müller J, Tsotsas E. 2015. Lotion distribution in wet wipes investigated by pore network simulation and X-ray micro tomography. *Transp. Porous Media* 107(2):449–68

Takahashi A, Häggkvist M, Li TQ. 1997. Capillary penetration in fibrous matrices studied by dynamic spiral magnetic resonance imaging. *Phys. Rev. E* 56(2):2035–42

Tejado A, Chen WC, Alam MN, van de Ven TGM. 2014. Superhydrophobic foam-like cellulose made of hydrophobized cellulose fibres. *Cellulose* 21:1735–43

Tejado A, van de Ven TGM. 2010. Why does paper get stronger as it dries? *Mater. Today* 13(9):42–49

Testoni GA, Kim S, Pisupati A, Park CH. 2018. Modeling of the capillary wicking of flax fibers by considering the effects of fiber swelling and liquid absorption. *J. Colloid Interface Sci.* 525:166–76

Van de Velde P, Protière S, Duprat C. 2021. Dynamics of drop absorption by a swelling fiber. *Soft Matter* 17:6168–75

van de Ven TGM. 2008. Capillary forces in wet paper. *Ind. Eng. Chem. Res.* 47(19):7250–56

Virozub A, Haimovich N, Brandon S. 2009. Three-dimensional simulations of liquid bridges between two cylinders: forces, energies, and torques. *Langmuir* 25(22):12837–42

Wang P, Zhou J, Xu B, Lu C, Meng QA, Liu H. 2020. Bioinspired anti-Plateau–Rayleigh-instability on dual parallel fibers. *Adv. Mater.* 32(45):2003453

Zhang K, Fang K, Bukhari MN, Xie R, Song Y, et al. 2020. The effect of ink drop spreading and coalescing on the image quality of printed cotton fabric. *Cellulose* 27(16):9725–36

Zhu L, Perwuelz A, Lewandowski M, Campagne C. 2008. Static and dynamic aspects of liquid capillary flow in thermally bonded polyester nonwoven fabrics. *J. Adhes. Sci. Technol.* 22(7):745–60